



1 **Improving the Sectional MOSAIC Aerosol models of WRF-Chem with the**
2 **revised Gridpoint Statistical Interpolation System and multi-wavelength aerosol**
3 **optical measurements: DAO-K experiment 2019 at Kashi, near the Taklamakan**
4 **Desert, northwestern China**

5
6 Wenyuan Chang¹, Ying Zhang², Zhengqiang Li², Jie Chen³, Kaitao Li²

7
8
9 ¹ State Key Laboratory of Atmospheric Boundary Layer Physics and Atmospheric Chemistry
10 (LAPC), Institute of Atmospheric Physics, Chinese Academy of Sciences, Beijing 100029,
11 China.

12
13 ² Institute of Remote Sensing and Digital Earth, Chinese Academy of Sciences, Beijing
14 100101, China

15
16 ³ National Meteorological Information Center, China Meteorological Administration, Beijing
17 100081, China

18
19
20
21
22
23 Corresponding authors:
24 Wenyuan Chang (changwy@mail.iap.ac.cn)
25 Zhengqiang Li (lizq@radi.ac.cn)

26
27



28 **Abstract**

29 The Gridpoint Statistical Interpolation data assimilation (DA) system was developed for the
30 four-size bin sectional Model for Simulating Aerosol Interactions and Chemistry (MOSAIC)
31 aerosol mechanism in the Weather Research and Forecasting-Chemistry (WRF-Chem) model.
32 The forward and adjoint operators for the aerosol optical depth (AOD) analysis were derived
33 from WRF-Chem aerosol optical code. We applied three-dimensional variational DA to
34 assimilate the multi-wavelength AOD, ambient aerosol scattering coefficient, and aerosol
35 absorption coefficient, measured by the sun-sky photometer, nephelometer, and aethalometer,
36 respectively. These were undertaken during a dust observation field campaign at Kashi in
37 northwestern China in April 2019. The results showed that the DA analyses decreased the low
38 biases in the model aerosols; however, it had had some deficiencies. Assimilating the surface
39 particle concentration increased the coarse particles in the dust episodes, but AOD, and the
40 coefficients for aerosol scattering and absorption, were still lower than observed values.
41 Assimilating aerosol scattering coefficient separately from AOD improved the two optical
42 quantities. However, it caused an overestimation of the particle concentrations at the surface.
43 Assimilating the aerosol absorption coefficient yielded the highest positive bias in the surface
44 particle concentration, aerosol scattering coefficient, and AOD. The positive biases in the DA
45 analysis were caused by the forward operator underestimating particle scattering and
46 absorption efficiency. As a compensation, the DA system increased particle concentrations
47 excessively so as to fit the observed optical values. The best overall improvements were
48 obtained from the simultaneous assimilation of the surface particle concentration and AOD.
49 The assimilation did not substantially change the aerosol chemical fractions. After DA, the
50 clear-sky aerosol radiative forcing at Kashi was -10.5 Wm^{-2} at the top of the atmosphere,
51 which was 46% higher than the background radiative forcing value.



52 **1. Introduction**

53 Data assimilation (DA) blends the information from observations with *a priori* background
54 fields from deterministic models to obtain an optimal analysis (Wang et al., 2001; Bannister,
55 2017). With lagged emission inventories and unsatisfactory model chemistry mechanisms,
56 there are notable discrepancies between model aerosols and observed levels (He et al., 2017;
57 Chen L. et al., 2019). The DA technology incorporates aerosol measurements into the models
58 to optimize emissions (Peng et al., 2017; Ma et al., 2019), and cyclically updates the
59 background fields in forecasts. This effectively improves the air quality forecasts in China
60 (Bao et al., 2019; Cheng et al., 2019; Feng et al., 2018; Hong et al., 2020; Liu et al., 2011;
61 Pang et al., 2018; Peng et al., 2018; Xia et al., 2019a, 2019b).

62
63 Variational DA minimizes the distant scalar function measuring the misfit between model
64 states and a set of observations in each assimilation window. An effective variational DA
65 requires an appropriate adjoint operator (or Jacobian matrix), which describes the gradient or
66 sensitivity of the observed parameter to the control variable (Wang et al., 2001; Bannister
67 2017). The adjoint operator is highly dependent on the types of assimilated observations and
68 the selection of control variables; it is also sometimes dependent on the aerosol mechanism.
69 For PM_{2.5} (particulate matter with dynamic radius less than 2.5 μm) DA, the adjoint operator
70 is the ratio of the PM_{2.5} concentration to composition of each aerosol (Pagowski et al., 2010).
71 For the aerosol optical depth (AOD) DA, the adjoint operator is generated through Mie theory
72 (Liu et al., 2011; Saide et al., 2013). With the development of aerosol mechanisms and the
73 growing body of novel aerosol observations from ground-based networks and satellites, an
74 appropriate adjoint operator is in demand.

75
76 The community gridpoint statistical interpolation (GSI) system (Wu et al., 2002; Purser et al.,
77 2003a, 2003b) is often used to modify regional aerosol simulations with three-dimensional
78 variational (3D-Var) DA. The official GSI (version 3.7 in this study) can incorporate
79 observations of surface particulate matter concentration and AOD to constrain the aerosols
80 simulated within the aerosol mechanism of Goddard Chemistry Aerosol Radiation and
81 Transport (GOCART, Liu et al., 2011; Pagowski et al., 2014). The tangent linear operator and
82 adjoint operator for AOD were determined using the Community Radiative Transfer Model
83 (CRTM). This GSI version incorporating the Moderate Resolution Imaging
84 Spectroradiometer (MODIS) AOD in East Asia (Liu et al., 2011), revealed the simultaneous
85 DA effects of PM_{2.5} and AOD in the continental United States (Schwartz et al., 2012). This
86 GIS was used to identify DA effects that weakened during running of the succeeding model
87 as the model error grew (Jiang et al., 2013), and assessed the radiative forcing of the aerosols
88 released by wildfires (Chen et al., 2014). This version of GSI was also utilized to improve air
89 quality forecasts in China by assimilating a variety of satellite AOD data retrieved from: the
90 Geostationary Ocean Color Imager (Pan et al., 2018); Visible Infrared Imaging Radiometer
91 Suite (Pang et al., 2018); Advanced Himawari-8 Imager (Xia et al., 2019a); and the Fengyun-
92 3A/medium-resolution spectral imager (Bao et al., 2019; Xia et al., 2019b).

93
94 Despite its capabilities, the GOCART mechanism is unable to simulate nitrate and secondary
95 organic aerosols (SOA), and the GOCART aerosol size distribution uses a bulk assumption



96 for radiative transfer calculation. Strictly speaking, the lack of aerosol components violates
97 the unbiased requirements for the model states in the DA system. Lack of size-segregated
98 aerosols may introduce a bias in the calculation of optical aerosols. The official GSI can
99 assimilate the surface particle concentration from the aerosol mechanism apart from
100 GOCART (Zang et al., 2016), but its AOD DA is tightly bound with the GOCART aerosols.
101 If one wished to use GSI to assimilate AOD for the other aerosol mechanisms, a compromise
102 solution was to integrate the map of the speciated aerosols of other mechanisms into that of
103 the GOCART aerosols. For example, Tang et al. (2017) used the official GSI to assimilate
104 MODIS AOD with the aerosols from the Community Multi-scale Air Quality Model
105 (CMAQ). They incorporated the map of the 54 aerosol components of CMAQ into the five
106 CRTM aerosols and repartitioned the mass increments of each CMAQ aerosol according to
107 the ratio of aerosol chemical components in the background field. This repartitioning is called
108 the “ratio approach.” Cheng et al. (2019) assimilated the lidar extinction coefficient profiles
109 measured in Beijing to modify the Weather Research and Forecasting-Chemistry (WRF-
110 Chem) Model for Simulating Aerosol Interactions and Chemistry (MOSAIC) aerosols. They
111 used the ratio approach to map eight MOSAIC aerosols based on five GOCART aerosols.
112 This mapping strategy is readily implemented but introduces inconsistent size-segregated
113 aerosol information (e.g., hygroscopicity and extinction efficiency) between the aerosol
114 model and the DA system. Because building a GSI system for a new aerosol mechanism is
115 quite technical, the official GSI for the GOCART aerosols is still a primary choice for recent
116 aerosol DA studies (Bao et al., 2019; Xia et al., 2019; Hong et al., 2020).

117
118 Because of the shortcomings, the official GSI has been extended to cooperate with other
119 aerosol mechanisms in WRF-Chem. The MOSAIC mechanism in WRF-Chem simulates
120 aerosol mass and number concentrations in either four- or eight-size bins. This sectional
121 aerosol mechanism involves nitrate chemistry and can simulate SOA with the volatility basis
122 set scheme. Saide et al. (2013) proposed a revised GSI version that performed variational DA
123 for the MOSAIC aerosols. The authors generated the adjoint operator code with the automatic
124 differentiation tool (ADT), TAPENADE v3.6. The ADT used the chain rule of derivative
125 calculus on the AOD source code in WRF-Chem. They assimilated multi-source AOD data
126 with the MOSAIC aerosols over continental United States and found that incorporating multi-
127 wavelength fine-mode AOD redistributed the aerosols’ particulate mass concentration sizes.
128 The revised GSI system assimilated Korean ground-based and geostationary satellite AOD
129 datasets to improve local aerosol simulations (Saide et al., 2014, 2020). Pang et al. (2020)
130 developed the official GSI to work with the Modal Aerosol Dynamics Model for Europe with
131 the Secondary Organic Aerosol Model (MADE/SORGAM) aerosols in WRF-Chem. The
132 authors used the WRF-Chem AOD code as the forward operator to calculate the essential
133 aerosol optical properties, which were then inputted to the CRTM adjoint operator. Because
134 aerosols were externally mixed in CRTM, the setting of the internal mixture per size bin in
135 WRF-Chem was not taken into account, and the AOD of each aerosol component was
136 calculated separately.

137
138 This study provides a solution to improve the capability of the GSI 3D-Var DA system for the
139 sectional MOSAIC aerosols in WRF-Chem. We designed the adjoint operator code for AOD



140 DA based on the WRF-Chem intrinsic aerosol optical subroutine (Fast et al., 2006), that is,
141 without using the ADT. The adjoint code is programmed based on the analytical equations of
142 the linear tangent model for AOD. As our revised GSI does not use the CRTM module, it
143 avoids the problem of needing to eliminate WRF-Chem aerosols characteristics (e.g., aerosol
144 mixture state and size distribution) to meet the CRTM input requirements. The forward and
145 adjoint operators are coordinated, since they are derived from the same WRF-Chem code, and
146 are written in a single subroutine, which is coupled to the GSI at the place of invoking CRTM
147 for the AOD calculation. In addition to AOD DA, our adjoint operator has two variants to
148 assimilate the aerosol scattering and absorption coefficients, measured using a nephelometer
149 and aethalometer, respectively.

150
151 This study verifies the effectiveness of our revised GSI system by incorporating multi-
152 wavelength aerosol optical observations that were measured during an international field
153 campaign, the Dust Aerosol Observation-Kashi, in April 2019 at Kashi city, neighboring the
154 Taklamakan Desert, northwestern China. This desert is the second largest globally, and is the
155 primary source of dust aerosols in East Asia. The dust from the desert affects the nearby
156 Tibetan Plateau (Ge et al., 2014; Jia et al., 2015; Zhao et al., 2020), air quality and climate in
157 East Asia (Huang et al., 2014), and the biogeochemical cycles in the western Pacific Ocean
158 (Calil et al., 2011). A successful DA analysis will help improve the local air quality forecast
159 and enhance our understanding of the environmental impacts of local dust storms. The
160 remainder of this paper is organized as follows. Section 2 describes the revised GSI system,
161 the experimental design, and the observed data. Section 3 presents the DA results when
162 assimilating different observations. Section 4 discusses the impact of DA on aerosol chemical
163 composition and aerosol direct radiative forcing. Finally, Section 5 provides the conclusions
164 and limitations that need further research.

165

166 **2. Methodology and Data**

167 **2.1 Forecast Model**

168 The background aerosol fields were simulated using the WRF-Chem model version 4.0 (Grell
169 et al., 2005; Fast et al., 2006). The model configurations included the Purdue Lin
170 microphysics scheme (Chen and Sun, 2002), the unified Noah land surface model (Tewari et
171 al., 2004), the Yonsei University scheme for planetary boundary layer meteorological
172 conditions (Hong et al., 2006), and the rapid radiative transfer model for general circulation
173 models (RRTMG) scheme for shortwave and longwave radiation (Iacono et al., 2008). The
174 gas-phase chemistry was simulated using the carbon bond mechanism (Zaveri and Peters,
175 1999), including aqueous-phase chemistry. The aerosol chemistry was simulated using the
176 MOSAIC mechanism (Zaveri et al., 2008), which simulated sulfate, nitrate, ammonium, black
177 carbon (BC), organic carbon (OC), sodium, calcium, chloride, carbonate, and other inorganic
178 matter (OIN, e.g., trace metals and silica). SOA was excluded from our experiments to
179 accelerate model integration. Although ignoring that SOA biased the model, the influence was
180 assumed to be small, based on low anthropogenic and biogenic emissions in the vicinity of the
181 desert. We performed the MOSAIC aerosol simulations with four-size bins (0.039–0.156 μm ,
182 0.156–0.625 μm , 0.625–2.500 μm , and 2.5–10.0 μm dry diameters). The sectional aerosol
183 data in the hourly model output were the aerosol dry mass mixing ratios of chemical



184 compositions, aerosol number concentration, and aerosol water content. The aerosol
185 compositions included hydrophilic particulates (i.e., SO_4^{2-} , NO_3^- , NH_4^+ , Cl^- , Na^+) and
186 hydrophobic particulates (i.e., BC, OC, and OIN). The dust emission was simulated using the
187 GOCART dust scheme (Ginoux et al., 2001). The dust mass was included in the OIN
188 concentration determination and aerosol optical calculation. The aerosol compositions were
189 externally mixed between the size bins and internally mixed in each size bin. The internal
190 mixing refractive index was the volume-weighted mean refractive index of each composition.

192 2.2 Assimilation System

193 The revised GSI DA system is based on the official GSI ([https://dtcenter.org/community-](https://dtcenter.org/community-code/gridpoint-statistical-interpolation-gsi)
194 [code/gridpoint-statistical-interpolation-gsi](https://dtcenter.org/community-code/gridpoint-statistical-interpolation-gsi), Wu et al., 2002; Liu et al., 2011; Schwartz et al.,
195 2012; Pagowski et al., 2014) version 3.7. The 3D-Var DA minimizes the cost function:

$$197 \quad J(\mathbf{x}) = \frac{1}{2}(\mathbf{x} - \mathbf{x}_b)^T \mathbf{B}^{-1}(\mathbf{x} - \mathbf{x}_b) + \frac{1}{2}(\mathbf{H}(\mathbf{x}) - \mathbf{y})^T \mathbf{R}^{-1}(\mathbf{H}(\mathbf{x}) - \mathbf{y})$$

198 (1)

199
200 where \mathbf{x} is the state vector composed of the model control variables; the subscript b denotes
201 that \mathbf{x} is the background state vector; \mathbf{y} is the vector of the observations; H is the forward
202 operator or observation operator that transfers the gridded control variables into the observed
203 quantities at the observation locations; and \mathbf{B} and \mathbf{R} are the background and observation error
204 covariance matrices, respectively.

205
206 The official GSI version only works with the GOCART aerosols for assimilating the surface-
207 layer $\text{PM}_{2.5}$ and PM_{10} (denoted as PM_x in the context) concentrations, and the 550 nm MODIS
208 AOD. Our revised GSI system assimilates PM_x concentrations, multi-wavelength aerosol
209 scattering/absorption coefficients, and AOD. Figure 1 shows the workflow of our DA system.
210 According to the AOD calculation in WRF-Chem, we can either choose the aerosol number
211 concentration (option 1), or aerosol mass concentration (option 2) as control variables. Option
212 1 is described in Li et al. (2020). In this study, we selected option 2, which is described in the
213 following subsections.

214
215 Figure 1

216 2.2.1 Control Variables

217 The control variables in this study were the mass mixing ratio of composition of each aerosol
218 per size bin, which corresponded to the WRF-Chem output data only. This set therefore
219 differed from previous studies that lumped aerosols per size bin as control variables. The
220 lumped aerosols avoided the burdensome task of specifying the background error statistics for
221 numerous aerosols (Li et al., 2013; Pagowski et al. 2014). Although our control variables
222 could have been further optimized, here we designed the control variable using only those that
223 substantially contributed to the total mass concentrations. In the case of Kashi situated near
224 the desert, the OIN was predominant, accounting for ~99% of the total particle mass
225 concentrations. The control variable could thus have exclusively comprised the OIN.



226 However, because we were curious about the response of aerosol chemical fractions in the
227 DA constraint, we set the control variables of five aerosol mass mixing ratios of SO_4^{2-} , NH_4^+ ,
228 OC, BC, and OIN per size bin. Nitrate, chlorine, and sodium had miniscule background
229 concentrations and remained the background values in the DA analysis. There were twenty
230 control variables in total for the four-size bin simulations, and the time cost for the DA
231 calculation for these variables was acceptable.

232
233 Our design of the control variables was different from the AOD assimilation in Saide et al.
234 (2013), with theirs being the natural logarithm of the total mass mixing ratio per size bin,
235 multiplied by the thickness of the model layer. As the high model layer had a significant layer
236 thickness with low aerosol concentrations, the multiplication offset the opposite effects of
237 increasing layer thickness versus decreasing concentrations with increase in altitude. This
238 prevented the addition of many modifications for the high model layers, where aerosols were
239 low in concentration. The logarithmic transformation was used to decrease the extensive
240 value range in the control variables caused by multiplication. Since the AOD value is often
241 smaller than one, this leads to a significant negative logarithm value and a relatively
242 unconstrained DA system. Saide et al. (2013) introduced two weak constraints in their cost
243 function to cut off the user-defined “extraordinarily high” and “extraordinarily low”
244 concentrations. However, neither the logarithmic transformation, nor the multiplication using
245 layer thickness was set in our DA system. Saide et al. (2013) repartitioned the increments of
246 the total mass per size bin for composition of each aerosol, with the background aerosol
247 chemical mass fractions. Our control variable was restricted to the WRF-Chem output
248 variable, and the DA system changed the composition of each aerosol per size bin, depending
249 on the aerosol background errors.

250
251 Consistent with the set by Pang et al. (2020), aerosol water content (AWC) was not one of the
252 control variables in our GSI. Otherwise, the AWC might have increased contrary to the
253 physical constraints for the loading of hydrophilic particles, and simply as a mathematical
254 artefact. The AWC was diagnosed according to the analyzed aerosol mass concentration and
255 the background relative humidity. The hygroscopic growth was calculated using the WRF-
256 Chem code coupled with the revised GSI.

257 258 **2.2.2 Adjoint Operator for PM_x**

259 The adjoint operator for PM_x is the gradient of the PM_x concentration to the aerosol chemical
260 mass concentration per size bin:

$$261 \frac{\delta[\text{PM}_x]}{\delta[C_{aer,k}]}, k = 1, \dots, n_{size} \quad (2)$$

262
263
264
265 where n_{size} is the number of size bins and is equal to four in this study; $[\cdot]$ denotes the mass
266 concentration ($\mu\text{g m}^{-3}$ for PM_x); $C_{aer,k}$ is the aerosol mass mixing ratio ($\mu\text{g kg}^{-1}$) of SO_4^{2-} ,
267 NH_4^+ , OC, BC, and OIN at the k -th size bin. The threshold of aerosol mass mixing ratio that
268 yields the non-zero adjoint operator is $0.01 \mu\text{g kg}^{-1}$. The $\text{PM}_{2.5}$ and PM_{10} are assimilated in the



269 same way. When the fine and coarse particles are assimilated simultaneously, we assimilate
 270 the concentration of PM_{2.5} and the coarse particulate (PM₁₀-PM_{2.5}).

271

272 2.2.3 Forward Operator for AOD in WRF-Chem

273 We used the original forward operator in WRF-Chem for the aerosol optical parameters (Fast
 274 et al., 2006). AOD is calculated as a function of wavelength according to Mie theory. The
 275 columnar AOD τ is the sum of layer AOD across the n_z model layers:

276

$$277 \quad \tau = \sum_{z=1}^{n_z} \tau_z = \sum_{z=1}^{n_z} \sum_{k=1}^{n_{size}} e_{ext,z,k} \cdot n_{z,k} \cdot H_z \quad (3)$$

278

279

280 where $e_{ext,z,k}$ is the extinction cross section of a single mixing particle in the k -th size bin at the
 281 z -th model layer, $n_{z,k}$ is the aerosol number concentration, and H_z is the layer thickness. The
 282 extinction cross section $e_{ext,z,k}$ of a wet particle with radius $r_{wet,z,k}$ is:

283

$$284 \quad e_{ext,z,k} = p_{ext,z,k} \cdot \pi \cdot r_{wet,z,k}^2 \quad (4)$$

285

286

287 where $p_{ext,z,k}$ is the extinction coefficient, given the desired mixing refractive indexes and the
 288 wet particle radius. The $p_{ext,z,k}$ is attained through the Chebyshev polynomial interpolation:

289

$$290 \quad p_{ext,z,k} = \exp \left\{ \sum_{j=1}^{n_{coef}} c_{ch}(j) \cdot c_{ext,z,k}(j) \right\} \quad (5)$$

291

292 where c_{ch} is the coefficient of n_{coef} order Chebyshev polynomials, $c_{ext,z,k}$ is the polynomial
 293 value for the extinction efficiency of the particle, which is an internal mixture of all aerosol
 294 compositions (i.e., the control variables plus nitrate, chlorine, sodium, and AWC). The radius
 295 in the AOD subroutine code is in a logarithmic transform to handle the broad particle size
 296 range from 0.039 μm to 10 μm . The exponential function in Eq. (5) transforms the logarithm
 297 radius back to the normal radius. The aerosol number concentration $n_{z,k}$, and the aerosol dry
 298 (wet) mass concentration $m_{i,z,k}$ have a linkage through the dry (wet) particle radius $r_{dry,z,k}$
 299 ($r_{wet,z,k}$) and the density ρ_i of each aerosol chemical composition:

300

$$301 \quad n_{z,k} = \sum_i^{n_{wet,aer}} \frac{m_{i,z,k}}{\rho_i} \cdot \frac{3}{4\pi \cdot r_{wet,z,k}^3} = \sum_i^{n_{dry,aer}} \frac{m_{i,z,k}}{\rho_i} \cdot \frac{3}{4\pi \cdot r_{dry,z,k}^3} \quad (6)$$

302

303

304 2.2.4 Adjoint Operator Developed for AOD

305 As per the forward operator in Eq. (3) in WRF-Chem, we developed the adjoint operator for
 306 AOD, which requires the derivative of τ in Eq. (3) to the mass concentration, $m_{i,z,k}$:



307
 308
$$\frac{\delta\tau}{\delta m_{i,z,k}} = \frac{\delta\tau_z}{\delta m_{i,z,k}} = \frac{\delta e_{ext,z,k} \cdot n_{z,k} \cdot H_z}{\delta m_{i,z,k}} + \frac{e_{ext,z,k} \cdot \delta n_{z,k} \cdot H_z}{\delta m_{i,z,k}} + \frac{e_{ext,z,k} \cdot n_{z,k} \cdot \delta H_z}{\delta m_{i,z,k}}$$

 309 (7)

310
 311 The first term on the righthand side of Eq. (7) indicates the change in AOD as the perturbation
 312 of extinction cross section. According to Eq. (4), considering that the particle radius is
 313 constant, $\delta e_{ext,z,k}$ is represented as:

314
 315
$$\delta e_{ext,z,k} = \delta p_{ext,z,k} \cdot \pi \cdot r_{wet,z,k}^2$$

 316 (8)

317
 318 where, $\delta ch(j) = 0$ assuming that the particle radius is constant. Equation (8) is expanded with
 319 the derivative of Eq. (5):

320
 321
$$\delta p_{ext,z,k} = p_{ext,z,k} \cdot \left\{ \sum_{j=1}^{n_{coef}} c_{ch}(j) \cdot \delta c_{ext,z,k}(j) \right\}$$

 322 (9)

323 By expanding $\delta c_{ext,z,k}$ in Eq. (9), we have:

324
 325
$$\delta c_{ext,z,k}(j) = \delta w_{00} \cdot E_{ext,00}(j) + \delta w_{01} \cdot E_{ext,01}(j) + \delta w_{10} \cdot E_{ext,10}(j) + \delta w_{11} \cdot E_{ext,11}(j)$$

 326 (10)

327
 328 where the four parameters of E_{ext} indicate the extinction efficiencies in the Mie table
 329 surrounding the point with the desired mixing refractive indexes, and the wet particle radius.

330 The changes in interpolation weights δw are determined as:

331
 332
$$\delta w_{00} = (v - 1)\delta u + (u - 1)\delta v \quad \delta w_{01} = (1 - v)\delta u - u\delta v$$

 333
$$\delta w_{10} = (1 - u)\delta v - v\delta u \quad \delta w_{11} = u\delta v + v\delta u$$

 334 (11)

335
 336 where

337
 338
$$u = \frac{R_{mix} - R_{low}}{R_{up} - R_{low}} \quad \delta u = \frac{\delta R_{mix}}{R_{up} - R_{low}}$$

 339
$$v = \frac{I_{mix} - I_{low}}{I_{up} - I_{low}} \quad \delta v = \frac{\delta I_{mix}}{I_{up} - I_{low}}$$

 340 (12)

341
 342 In Eq. (12), R_{mix} and I_{mix} are the aerosol volume-weighted mean real and imaginary refractive
 343 indices, respectively. R_{up} (I_{up}) and R_{low} (I_{low}) are the nearest upper and lower limits for R_{mix}
 344 (I_{mix}) in the Mie table. Considering $V_{wet,z,k}$ is the volume of all aerosol masses, the real and
 345 imaginary indices and their derivatives are:



346

$$347 \quad R_{mix,z,k} = \sum_i^{n_{wet,aer}} R_i \cdot \frac{m_{i,z,k}}{\rho_i \cdot V_{wet,z,k}} \quad \delta R_{mix,z,k} = \frac{R_i}{\rho_i \cdot V_{wet,z,k}} \cdot \delta m_{i,z,k}$$

$$348 \quad I_{mix,z,k} = \sum_i^{n_{wet,aer}} I_i \cdot \frac{m_{i,z,k}}{\rho_i \cdot V_{wet,z,k}} \quad \delta I_{mix,z,k} = \frac{I_i}{\rho_i \cdot V_{wet,z,k}} \cdot \delta m_{i,z,k}$$

349 (13)

350

351 where

$$352 \quad V_{wet,z,k} = \sum_i^{n_{wet,aer}} \frac{m_{i,z,k}}{\rho_i}$$

353 (14)

354

355 Put Eq. (10), Eq. (11) into Eq. (9) leads to:

356

$$357 \quad \delta p_{z,k} = [(v-1)\alpha_{00} + (1-v)\alpha_{01} - v\alpha_{10} + v\alpha_{11}]\delta u +$$

$$358 \quad [(u-1)\alpha_{00} - u\alpha_{01} + (1-u)\alpha_{10} + u\alpha_{11}]\delta v$$

359 (15)

360

360 where

$$361 \quad \alpha_{00} = p_{ext,z,k} \cdot \sum_{j=1}^{n_{coef}} c_{ch}(j) \cdot E_{ext,00}(j) \quad \alpha_{01} = p_{ext,z,k} \cdot \sum_{j=1}^{n_{coef}} c_{ch}(j) \cdot E_{ext,01}(j)$$

$$362 \quad \alpha_{10} = p_{ext,z,k} \cdot \sum_{j=1}^{n_{coef}} c_{ch}(j) \cdot E_{ext,10}(j) \quad \alpha_{11} = p_{ext,z,k} \cdot \sum_{j=1}^{n_{coef}} c_{ch}(j) \cdot E_{ext,11}(j)$$

363 (16)

364

365 The first term on the righthand side of Eq. (7) is determined using Eq. (8) and Eq. (15). The
 366 second term on the righthand side of Eq. (7) indicates the linkage of the aerosol number and
 367 mass concentrations. It is the derivative of Eq. (6) by assuming a constant radius:

368

$$369 \quad \delta n_{z,k} = \frac{3 \cdot \delta m_{i,z,k}}{4\pi \cdot r_{dry,z,k}^3 \cdot \rho_i}$$

370 (17)

371

372 The third term on the righthand side of Eq. (7) contains the derivative of the layer thickness to
 373 the concentrations in this layer. This indicates that the light attenuation length based on per
 374 unit concentration, which can be intuitively represented by the ratio of layer thickness to the
 375 aerosol mass concentration in this layer. Putting Eq. (8) and Eq. (17) into Eq. (7), we have the
 376 original formula of the adjoint operator for AOD for the aerosol mass concentration:

377

378



$$\begin{aligned}
 379 \quad \frac{\delta\tau}{\delta m_{i,z,k}} &= \frac{\delta\tau_z}{\delta m_{i,z,k}} = \frac{\delta e_{ext,z,k} \cdot n_{z,k} \cdot H_z}{\delta m_{i,z,k}} + \frac{e_{ext,z,k} \cdot \delta n_{z,k} \cdot H_z}{\delta m_{i,z,k}} + \frac{e_{ext,z,k} \cdot n_{z,k} \cdot \delta H_z}{\delta m_{i,z,k}} = \\
 380 \quad & \{[(v-1)\alpha_{00} + (1-v)\alpha_{01} - v\alpha_{10} + v\alpha_{11}] \cdot \frac{\pi \cdot r_{wet,z,k}^2 \cdot R_i \cdot n_{z,k} \cdot H_z}{\rho_i \cdot V_{z,k} \cdot (R_{up,z,k} - R_{low,z,k})} + \\
 381 \quad & [(u-1)\alpha_{00} - u\alpha_{01} + (1-u)\alpha_{10} + u\alpha_{11}] \cdot \frac{\pi \cdot r_{wet,z,k}^2 \cdot I_i \cdot n_{z,k} \cdot H_z}{\rho_i \cdot V_{z,k} \cdot (I_{up,z,k} - I_{low,z,k})} + \\
 382 \quad & \frac{3e_{ext,z,k} \cdot H_z}{4\pi \cdot r_{dry,z,k}^3 \cdot \rho_i} + \frac{e_{ext,z,k} \cdot n_{z,k} \cdot H_z}{m_{i,z,k}} \} \cdot \beta \\
 383 & \\
 384 & \\
 385 & \hspace{15em} (18)
 \end{aligned}$$

386 where β is the factor that changes the unit of mass from $\mu\text{g kg}^{-1}$ to $\mu\text{g m}^{-3}$. The last righthand
 387 term in Eq. (18) may not have a quick convergence in the DA outer loops because the aerosol
 388 mass concentration $m_{i,z,k}$ in the denominator often has a low bias, which introduces an error
 389 into the adjoint operator. The error is amplified by the layer thickness H_z in the numerator.
 390 Thus, the adjoint operator of Eq. (18) cannot lead to a stable analysis. For this reason, we
 391 changed the adjoint operator to account for the columnar mean aerosol extinction coefficient
 392 which is described as follows:

$$\begin{aligned}
 394 \quad \frac{\delta(\overline{e_{ext} \cdot n})}{\delta m_{i,z,k}} &= \frac{H_z}{\sum H_z} \cdot \frac{\delta(e_{ext,z,k} \cdot n_{z,k})}{\delta m_{i,z,k}} = \frac{H_z}{\sum H_z} \cdot \left[\frac{\delta e_{ext,z,k} \cdot n_{z,k}}{\delta m_{i,z,k}} + \frac{e_{ext,z,k} \cdot \delta n_{z,k}}{\delta m_{i,z,k}} \right] = \\
 395 \quad & \{[(v-1)\alpha_{00} + (1-v)\alpha_{01} - v\alpha_{10} + v\alpha_{11}] \cdot \frac{\pi \cdot r_{wet,z,k}^2 \cdot R_i \cdot n_{z,k}}{\rho_i \cdot V_{z,k} \cdot (R_{up,z,k} - R_{low,z,k})} + \\
 396 \quad & [(u-1)\alpha_{00} - u\alpha_{01} + (1-u)\alpha_{10} + u\alpha_{11}] \cdot \frac{\pi \cdot r_{wet,z,k}^2 \cdot I_i \cdot n_{z,k}}{\rho_i \cdot V_{z,k} \cdot (I_{up,z,k} - I_{low,z,k})} + \\
 397 \quad & \frac{3e_{ext,z,k}}{4\pi \cdot r_{dry,z,k}^3 \cdot \rho_i} \} \cdot \beta \cdot \frac{H_z}{\sum H_z} \\
 398 & \\
 399 & \hspace{15em} (19) \\
 400 &
 \end{aligned}$$

401 In Eq. (19), the operator is based on the extinction coefficient at each layer, weighted by the
 402 layer thickness normalized to the total model layer thickness. Correspondingly, the AOD
 403 observations and AOD observation error are divided by the total layer thickness at the
 404 observation location. Equation (19) is the final adjoint operator for AOD DA in this study.

406 2.2.5 Adjoint Operator Developed for Surface Aerosol Attenuation Coefficients

407 The aerosol scattering and absorption coefficients measured by the nephelometer and
 408 aethalometer, respectively, are similar to the aerosol extinction coefficient at the surface in
 409 Eq. (19). Neither of the two coefficients address the layer thickness. The adjoint operator for
 410 the aerosol scattering coefficient measured by nephelometer is described as follows:



411
 413
$$\frac{\delta(e_{sca,1,k} \cdot n_{1,k})}{\delta m_{i,1,k}} = \{[(v-1)\alpha_{00} + (1-v)\alpha_{01} - v\alpha_{10} + v\alpha_{11}] \cdot \frac{\pi \cdot r_{wet,1,k}^2 \cdot R_i \cdot n_{1,k}}{\rho_i \cdot V_{1,k} \cdot (R_{up,1,k} - R_{low,1,k})}$$

 414
$$+ \frac{3e_{sca,1,k}}{4\pi \cdot r_{dry,1,k}^3 \cdot \rho_i}\} \cdot \beta$$

 412
 415 (20)

416
$$\alpha_{00} = p_{sca,1,k} \cdot \sum_{j=1}^{n_{coef}} c_{ch}(j) \cdot E_{sca,00}(j) \quad \alpha_{01} = p_{sca,1,k} \cdot \sum_{j=1}^{n_{coef}} c_{ch}(j) \cdot E_{sca,01}(j)$$

 417
$$\alpha_{10} = p_{sca,1,k} \cdot \sum_{j=1}^{n_{coef}} c_{ch}(j) \cdot E_{sca,10}(j) \quad \alpha_{11} = p_{sca,1,k} \cdot \sum_{j=1}^{n_{coef}} c_{ch}(j) \cdot E_{sca,11}(j)$$

 418
 419 (21)
 420

421 The adjoint operator for the aerosol absorption coefficient measured by aethalometer is
 422

424
$$\frac{\delta(e_{abs,1,k} \cdot n_{1,k})}{\delta m_{i,1,k}} = \{[(u-1)\alpha_{00} - u\alpha_{01} + (1-u)\alpha_{10} + u\alpha_{11}] \cdot \frac{\pi \cdot r_{wet,1,k}^2 \cdot I_i \cdot n_{1,k}}{\rho_i \cdot V_{1,k} \cdot (I_{up,1,k} - I_{low,1,k})}$$

 425
$$+ \frac{3e_{abs,1,k}}{4\pi \cdot r_{dry,1,k}^3 \cdot \rho_i}\} \cdot \beta$$

 423
 426 (22)

427
$$\alpha_{00} = p_{abs,1,k} \cdot \sum_{j=1}^{n_{coef}} c_{ch}(j) \cdot E_{abs,00}(j) \quad \alpha_{01} = p_{abs,1,k} \cdot \sum_{j=1}^{n_{coef}} c_{ch}(j) \cdot E_{abs,01}(j)$$

 428
$$\alpha_{10} = p_{abs,1,k} \cdot \sum_{j=1}^{n_{coef}} c_{ch}(j) \cdot E_{abs,10}(j) \quad \alpha_{11} = p_{abs,1,k} \cdot \sum_{j=1}^{n_{coef}} c_{ch}(j) \cdot E_{abs,11}(j)$$

 429
 430 (23)
 431

432 where the symbols have the same meaning as before. The subscript one denotes the surface
 433 layer, while. *sca* and *abs* denote “scattering” and “absorption,” respectively.
 434

435 As shown in the adjoint operators, the gradients of the aerosol mass concentrations rely on the
 436 aerosol number concentration; meanwhile, the number concentration is estimated according to
 437 the mass concentration and the particle radius. The two concentrations are intertwined in the
 438 DA system, indicating the nonlinearity of the adjoint operator. This nonlinearity is handled
 439 with a succeeding minimization of the cost function within the GSI. That is, the cost function
 440 is first minimized with the number concentration in the background field, and the number
 441 concentration is updated with the first analyzed aerosol mass concentrations. In the second
 442 minimization, the number concentration assessed in the first analysis constructs a new adjoint



443 operator value, resulting in a new analysis of mass concentrations. This iterative process is
444 denoted as the “outer loop,” which is repeated several times to attain the final analysis
445 (Massart et al., 2010). We used ten iterations to handle the nonlinearity in the adjoint
446 operator. The WRF-Chem AOD code is coupled into the GSI subroutine at the place of
447 invoking CRTM. The AOD and the adjoint operators of Eq. (19), Eq. (20), and Eq. (22) are
448 simultaneously determined in a single subroutine, which is cyclically invoked in the outer
449 loops within the GSI.

450

451 **2.3 Background Error Covariance (BEC)**

452 Many aerosol DA studies used the National Meteorological Center (NMC) method (Parrish
453 and Derber, 1992) to model the BEC matrix. The NMC method uses long-term archived
454 weather data that are created in the forecast cycles. It computes the statistical differences
455 between two forecasts with different leading lengths (e.g., 24 h and 48 h), but which are valid
456 at the same time. The NMC method is workable because solving global weather forecasts is
457 an initial value problem of mathematical physics. That is, a slight difference in the initial
458 atmospheric state would lead to a substantially different prediction, because of the chaos in
459 the atmosphere. However, a regional model is a boundary value problem. Meteorological
460 reanalysis data drive the regional chemistry simulation, and the driving data quality affects the
461 simulation (Giorgi and Mearns, 1999). The WRF-Chem simulations in the NMC method only
462 reflected the influences of using different initial conditions. As the model runs, the influence
463 of the initial conditions becomes weak, while the influence of lateral boundary conditions
464 always takes effect. Because the same reanalysis data drive the paring regional model
465 simulations, the following lateral boundary conditions for the simulations of the two leading-
466 lengths are similar. This leads to a limited regional model difference when using the NMC
467 method. We speculate that the NMC method cannot fully represent the model biases in
468 emission inventories and model chemistry, and it underestimates the aerosol error in WRF-
469 Chem.

470

471 Some aerosol DA studies have created background error variance using the ensemble
472 simulations by randomly disturbing model lateral boundary conditions and surface emissions
473 (Peng et al., 2017; Ma et al., 2020). The ensemble experiments better represent the model
474 error, but significantly increase the computational burden. Here, we used the standard
475 deviation of hourly aerosol concentrations in April in the background field (first guess field)
476 to represent the background error variance. The rationale of this approach is that the Tarim
477 Basin acts as a “dust reservoir” and traps dust particles for a period, before being carried long-
478 distance by wind (Fan et al., 2020). The model bias in dust dominates the model aerosol error,
479 and is correlated with the aerosol variation as the weather fluctuates. The model bias is small
480 on clear days when the aerosol concentration is low. Conversely, the bias is large when the
481 mean concentration is high: that is, on heavily-polluted days. Because the mean aerosol
482 concentration correlated positively with the aerosol variation, we used the standard deviation
483 of aerosol concentration to represent the background aerosol error. This approach was similar
484 to Sič et al. (2016), who set a percentage of the first guess field for the background error
485 variance. Our approach prioritizes DA modification of aerosols which have high background
486 mean concentrations.



487
488 We calculated the statistics of the background error, including the aerosol standard deviation
489 and the horizontal and vertical correlation length scales, using the GENerate the Background
490 Errors (GEN-BE) software (Descombes et al., 2015), based on the one-month hourly aerosol
491 concentrations in WRF-Chem. We obtained the statistics of four static BECs for the four DA
492 analysis hours (i.e., 00:00, 06:00, 12:00, and 18:00 UTC), respectively. The DA procedures
493 for the April 2019 data repeatedly use the statistics of the background error at the
494 corresponding analysis time. A usual strategy to enrich the samples of model results for
495 calculating the statistics is to gather model grid points with similar characteristics of the
496 atmosphere, referred to as “binning.” The statistics are spatially averaged over the binned grid
497 points. The default strategy in the GEN_BE for GSI is latitude-binning, which creates a
498 latitude-dependent error correlation function (Figure 2a). The latitude binning is generally
499 used for latitude flow dependency and works for large and global domains (Wu et al., 2002).
500 However, we found that using the latitude-binning strategy overestimated the surface PM_x
501 concentration when assimilating aerosol optical observations. One reason for this was related
502 to the model bias in particle extinction efficiency, as discussed in Section 3.3. Another
503 plausible reason is related to the vertical profile of the background model error. The
504 maximum dust error occurred at the surface of the desert (Figure 2e) because of the local dust
505 emission sources, but the maximum error at Kashi was at the dust transporting layer above the
506 surface (Figure 2d). Owing to the vast extent of the Taklamakan Desert, the latitude-binning
507 suppressed the local error characteristics at Kashi, and led to a vertical error profile (Figure
508 2c) similar to that over the desert (Figure 2e).
509
510 For this reason, we used the standard deviation of the control variable for the OIN component
511 at each model grid to replace the latitude-binning standard deviation. The standard deviation
512 for the other compositions and the horizontal and vertical correlation length scales were
513 calculated based on the latitude-binning data. Figure 3 shows the background error statistics
514 generated by the GEN_BE software, which provided the input to the GSI. Anthropogenic
515 aerosol compositions showed vertical error profiles, greatest at the surface (Figures 3a-d). The
516 OIN component showed high background errors in the third and fourth particle sizes at the
517 transporting layer above the surface (Figure 3e). The aerosol compositions related to
518 anthropogenic emissions (i.e., sulfate, ammonium, OC, and BC, referred to here as
519 ‘anthropogenic aerosols’) had maximum errors in the second particle size. The background
520 error for OIN composition was higher than that for anthropogenic aerosols by a factor of two
521 or three, because of the high background dust concentration in the city.
522
523 The horizontal and vertical correlation length scales determine the range of observation
524 innovations spreading from the observation locations. The horizontal influences had small
525 changes in altitude within the lowest 15 model layers (below a height of ~5 km) (Figures 3f-
526 j), indicating that the dust transport layer was well-mixed in the lower atmosphere. This deep
527 dust layer was consistent with the dust simulation by Meng et al. (2019). They showed that
528 the dust in spring was vertically mixed in a thick boundary layer to a height of 3–5 km in the
529 Tarim Basin. The vertical correlation length scales first increased from low values at the
530 surface, to high values at ~2.5 km in height (for the 8–9 layers), indicating that strong winds



531 yielded intense aerosol upward flux. The vertical correlation length scale quickly decreased
532 from the maximum value, with further increase in altitude corresponding to the large particle
533 gradient at the upper edge of the transporting layer. The latter was associated with laminar air
534 motion during the dust storm.

535
536 The background model errors were independent of particle size, which would have tended to
537 accumulate the DA modification in a single size bin that had the maximum background error
538 (e.g., the OIN in the fourth particle size). To avoid excessive accumulation of increments in a
539 single size bin, we added a one-dimensional recursive filter for the background covariances of
540 control variables across the size bins within the GSI. The inter-size bin correlation length
541 scale was two bin units, as per the setting of Saide et al. (2013).

542

Figure 2, Figure 3

543

544 2.4 Observational Data and Errors

545 The Dust Aerosol Observation–Kashi field campaign was performed at Kashi from
546 00:00UTC 25 March to 00:00 UTC 1 May 2019. The aerosol observations used for our DA
547 analysis included: (1) the multi-wavelength AOD measured by the sun-sky photometer
548 (Cimel CE318); (2) the multi-wavelength aerosol scattering and absorption coefficients at the
549 surface, measured with a nephelometer (Aurora 3000) and aethalometer (Magee AE-33),
550 respectively, during the campaign; and (3) the routine hourly $PM_{2.5}$ and PM_{10} observations
551 measured by the China National Environmental Monitoring Center. Please refer to Li et al.
552 (2020) for more details about the field campaign.

553

554 Table 1 summarizes the observation periods, the wavelengths of the aerosol optical data, and
555 the observation errors. The multi-wavelength data of each type of observation were
556 assimilated simultaneously. The observation errors of PM_x consisted of the measurement error
557 (e_1) and the representative error (e_2). The observation error of AOD was a constant value of
558 0.01, which was further divided by the total model layer thickness in GSI. It is difficult to
559 determine instrumental errors in nephelometers and aethalometers, and we empirically set
560 their instrumental errors to 10 Mm^{-1} , equivalent to the magnitude of the Rayleigh extinction
561 coefficient. The observational errors were uncorrelated, with \mathbf{R} being a diagonal matrix.

562

Table 1

563

564 2.5 Experimental Design

565 The WRF-Chem simulations were configured in a two-nested domain centered at 82.9°E ,
566 41.5°N . The coarse domain was a 120×100 (west-east \times north-south) grid with a horizontal
567 resolution of 20 km that covered the Taklamakan Desert, and the fine domain was an 81×61
568 grid with a resolution of 5 km, focusing on Kashi and environs (Figure 4a). Both domains had
569 41 vertical levels extending from the surface to 50 hPa. The two domains were two-way
570 coupled. The parent domain covered the entire dust emission source, providing dust transport
571 fluxes at the lateral boundaries of the fine domain. The aerosol radiative effect was set to
572 provide feedback on the meteorology. The indirect effect of aerosols was not set in the



573 experiments. Initial and lateral boundary meteorological conditions for WRF-Chem were the
574 one-degree resolution of the National Centers for Environmental Prediction Final Analysis
575 data created by the Global Forecast System model. The meteorological lateral boundary
576 conditions for the coarse domain were updated every six hours, and were linearly interpolated
577 between the updates in WRF-Chem. We did not set the chemical boundary conditions for the
578 coarse domain. The Multiresolution Emission Inventory of China (MEIC) for 2010
579 (www.meicmodel.org) provided anthropogenic emission levels. The biogenic emission levels
580 were estimated online using the Model of Emissions of Gases and Aerosols from Nature
581 (Guenther et al., 2006). Wildfire emissions were not set in the experiments.

582
583 We conducted a one-month WRF-Chem simulation for April 2019, starting at 00:00 UTC 27
584 March and discarding the first five days for spin-up. The revised GSI system modified the
585 aerosols in the fine domain at 00:00, 06:00, 12:00, and 18:00 UTC on each day, starting from
586 00:00 UTC 1 April until the end of the month. We assimilated the observations four times a
587 day because the reanalyzed meteorological data were available for the four time slices, which
588 facilitated the model restarting from the DA analyses. The hourly PM_x observations were
589 assimilated at the exact time of analysis. The observed AOD and aerosol scattering/absorption
590 coefficients were assimilated when they fell within ± 3 h, centered at the time of analysis.
591 Table 2 shows the DA experiments. The literal meanings of the experimental names denote
592 the observations that were individually or simultaneously assimilated. To study the impact of
593 DA on aerosol direct radiative forcing (ADRF), we restarted the WRF-Chem model from
594 each DA analysis, which then ran to the next analysis time. Each running performed the
595 radiation transfer calculation both with, and without aerosols, respectively. The irradiance
596 difference between the two pairing calls was aerosol radiative forcing. Section 4.2 shows the
597 DA effects on the clear-sky ADRF values.

598

Table 2, Figure 4

599

600 3. Results

601 3.1 Evaluation of Control Experiment

602 Table 2 shows the monthly mean values and correlations between the observed data and the
603 model results. The statistical values were based on the pairing data between the model results
604 and the observations. Figures 6–9 show the surface PM_x concentrations, aerosol scattering,
605 absorption coefficients, and AOD when assimilating the observations at 00:00, 06:00, 12:00,
606 and 18:00 UTC each day in April.

607

608 Kashi is in the junction between the Tian Shan Mountains to the west and the Taklamakan
609 Desert to the east (Figure 5a). In the Tarim Basin, the prevailing surface wind is easterly or
610 northeasterly, which raises dust levels and carries the particles westward (Figure 5b). An
611 intense dust storm hit the city at noon on 24 April 2019, with a peak PM_{10} concentration
612 exceeding $3,000 \mu\text{g m}^{-3}$. The dust storm travelled across the northern part of the desert and
613 carried the dust particles to Kashi and the mountainous area (Figure 5c, d). A few mild dust
614 storms occurred at Kashi on April 3–5, April 8–11, and April 14–17 (Figure 6b), and the
615 maximum PM_{10} concentrations were in the range of $400\text{--}600 \mu\text{g m}^{-3}$. The time series of $PM_{2.5}$,



616 aerosol scattering/absorption coefficient, and AOD showed patterns, similar to those for PM₁₀
617 (Figure 6).

618

619 WRF-Chem captured the main dust episodes, but significantly underestimated the aerosols at
620 Kashi (Table 2). The background monthly mean concentrations of PM_{2.5} and PM₁₀ were half
621 of the observed values, with a low correlation ($R < 0.3$). The simulated dust storm on 24 April
622 was a mild dust event and had a maximum PM₁₀ of $\sim 300 \mu\text{g m}^{-3}$, one-tenth of the observed
623 value. The model lowered the aerosol scattering/absorption coefficients and AOD by 50–
624 90%.

625

626 The OIN component accounted for the model bias in PM₁₀ on dusty days. Zhao et al. (2020)
627 proposed that the GOCART scheme reproduced dust emission fluxes under conditions of
628 weak wind erosion but underestimated the emissions in conditions of strong wind erosion. We
629 did not assimilate meteorology. The model bias in the surface wind introduces errors in dust
630 emission, and places bias on the number of dust particles entering the city. In the non-dust
631 days, for example, on 20 April, the model hourly PM_{2.5} was 10–50% of the observed data
632 levels. The simulated anthropogenic aerosols were probably too low to be reasonable for this
633 city. The residential sector is a major source of anthropogenic emissions, including PM_{2.5}, BC,
634 and OC, particularly in the developing western area. The latter sector accounts for 36–82% of
635 these emissions, according to the MEIC emission inventory (Li et al., 2017). The sector is the
636 primary source of uncertainty in anthropogenic emissions inventories in China. We speculated
637 that the low bias in anthropogenic emissions could be significant for Kashi, resulting in low
638 anthropogenic aerosols in the model.

639

Figure 5

640

641 3.2 Assimilating PM_{2.5} and PM₁₀ Concentrations

642 Simultaneous assimilation of the observed PM_x (DA_PM_x) improved both the fine and coarse
643 particle concentrations, with a substantial improvement in the third and fourth particle sizes of
644 the OIN composition (Figure 11e). The analyzed monthly mean PM₁₀ increased to $331.2 \mu\text{g}$
645 m^{-3} , with a high correlation of 0.99. The analyzed monthly mean PM_{2.5} was improved to 70.3
646 $\mu\text{g m}^{-3}$, although it was still lower than the observed levels, with a high correlation of 0.86.

647 The low bias in PM_{2.5} was mainly in the dust storm on 24–25 April (Figure 6a). This indicates
648 that the DA system preferentially modified the coarse particle concentrations because the
649 coarse particles were assigned with a high background model error according to our BEC
650 modeling strategy. Intuitively, this modification that mainly focused on the highest
651 concentration of coarse particles was reasonable. It decreased the model biases by raising the
652 heaviest loading aerosols. As the particle concentration increased, the aerosol scattering
653 coefficient increased to 158.9 Mm^{-1} , with a high correlation of 0.86. However, the
654 improvements in the analyzed absorption coefficients and AOD were insufficient (Figures 6d-
655 e). The analyzed absorption coefficient was 12.2 Mm^{-1} , 85% lower than observed levels, with
656 a low correlation of 0.33. The analyzed AOD showed a monthly mean value of 0.31, 56%
657 lower than observed levels, with a low correlation of 0.37.

658



659 Figure 10 shows the diurnal concentrations of PM_{10} in the analyses in April. The observed
660 PM_{10} showed a substantial variation at 18:00 UTC, the (local midnight). This substantial
661 nocturnal variation was partly owing to the dust storm that started on 24 April and ended the
662 next day. This midnight variation was also related to a nocturnal low-level jet. Ge et al.
663 (2016) pointed out that there was a nocturnal low-level jet at a height of 100–400 m, with a
664 wind speed of 4–10 $m\ s^{-1}$ throughout the year in the Tarim Basin. They stressed that the low-
665 level jet broke down in the morning, transporting its momentum toward the surface, and
666 increased dust emissions. The nocturnal low-level jet increased the possibility of dust
667 particles moving towards the city at night, causing a high PM_{10} variation at 18:00 UTC. The
668 diurnal changes in the DA analyses followed the observed levels, but had higher mean values
669 (Figure 10a).

670

671 3.3 Assimilating AOD

672 Assimilating AOD (DA_AOD) improved the monthly mean AOD to 0.63, with a high
673 correlation of 0.99 (Figure 7e). The monthly mean $PM_{2.5}$ was improved to $85.0\ \mu g\ m^{-3}$, quite
674 close to the observed level, but the analyzed PM_{10} was $716.9\ \mu g\ m^{-3}$, which was more than
675 double the observed value. The DA system improved the AOD at the price of deteriorating
676 the data quality of surface particle concentrations, opposite to the result when assimilating
677 PM_x . Surface particle overestimations have been reported in previous studies (Liu et al., 2011;
678 Ma et al., 2020; Saide et al., 2020). Ma et al. (2020) assimilated ground-based lidars and
679 $PM_{2.5}$ simultaneously in eastern China using the WRF-Chem/DART (Data Assimilation
680 Research Testbed). They claimed that WRF-Chem underestimated the AOD and low-level
681 aerosol extinction coefficient because the model had a low bias in relative humidity, which
682 led to less AWC and lowered the single-particle extinction. As a compensation, the DA
683 system overestimated the total particle concentration to fit the observed AOD value. In the
684 arid area of Kashi, PM_{10} was strongly overestimated when assimilating AOD. We speculate
685 that WRF-Chem also lowers the dust extinction efficiency.

686

687 Table 3 shows the ratios of the AOD and aerosol scattering/absorption coefficients to the
688 surface PM_{10} concentrations in the DA_ PM_x experiment. The other DA experiments yielded
689 almost similar results. This shows that the ratio of AOD to PM_{10} in the background model
690 result was only one-third of the observed levels. This low ratio indicated a model low bias in
691 particle scattering/absorption efficiency and imposed the DA system to overestimate the PM_{10}
692 to fit the observed AOD data. The low bias is related to the aerosol optical module, which is
693 based on Mie theory in WRF-Chem. First, the simulations used four-size bin particle
694 segregation. This coarse size representation aggregated many aerosols in the accumulation
695 mode. Because small particles have a strong of light attenuation capability, according to the
696 Mie theory, too many coarse particles would not effectively increase the AOD. Saide et al.
697 (2020) linked the aerosol optics to the size bin representation (from 4 to 16 bins) for hazes in
698 South Korea. They showed that WRF-Chem underestimated the dry aerosol extinction, and
699 the underestimation could be relieved when using a finer size bin than four. Okada and Kai
700 (2004) found that the dust particle radius in the Taklamakan Desert was in the range of 0.1–4
701 μm , indicating the dominant fine-mode particles in the desert. Using the four-size bin would
702 simultaneously obtain better analyses of both AOD and PM_x . Second, the dust particles are



703 irregular in shape (Okada and Kai, 2004), while the spherical particle is a common
704 assumption for the aerosol optics in the Mie theory in current models, which is an essential
705 source of uncertainty in the forward operator of WRF-Chem when the assumption of
706 spherical particles for dust fails.

707
708 Another reason for the low ratio of AOD to PM_{10} is related to our approach for modeling
709 BEC. It is important to remember that our BEC represents the possible error effects owing to
710 model bias in aerosols. The coarse particle accounts for a large mass portion of PM_x , and its
711 bias dominates the model error. However, we cannot say that this background error
712 assessment is unbiased. As our BEC gave a high background error to the coarse particle for its
713 sufficient concentration, the DA system tended to increase PM_{10} , which was not as effective
714 in increasing AOD as $PM_{2.5}$. If the background error of the coarse particle were too high, the
715 BEC would falsely lower the ratio of AOD to PM_{10} in the analysis.

716
717 To reduce the overestimate in PM_x concentrations, we set the gridded standard deviation for
718 the OIN for Kashi in place of the latitude-binning standard deviation, as discussed in Section
719 2.3. Figure 12 shows the analyzed vertical profiles of PM_x concentrations. Higher
720 concentrations were observed in the low atmosphere than at the surface. These vertical error
721 profiles decreased the surface particles and tended to increase the ratio, contrary to the effects
722 of low model bias in particle extinction efficiency and the possible high bias in the BEC
723 values of coarse particles. For the net effect of the compensation, the ratio in the analysis was
724 still almost equivalent to the background value (Table 3). That is, our tuned BEC vertical
725 profile at Kashi, to some extent canceled out the effects of other model error sources (e.g., the
726 positive bias in the coarse particle of BEC, and the low bias in extinction efficiency) but was
727 not sufficient to increase the ratio to the observed value. Finer aerosol size representation and
728 a better advanced aerosol optical calculation for dust are essential solutions.

729
730 Because the DA system overestimated the aerosol number concentration, resulting in a
731 positive bias in PM_{10} , the analyzed aerosol scattering coefficient was overestimated up to
732 280.1 Mm^{-1} , 37% higher than the observed value. In contrast, the analyzed absorption
733 coefficient was 23.1 Mm^{-1} , 72% lower than the observed value. This indicates that WRF-
734 Chem strongly underestimated the single-particle absorption efficiency, and the low bias was
735 too strong to be compensated by the overestimated aerosol number concentration.

736
737 Assimilating the AOD increased the diurnal variation in the DA analyses. There was a higher
738 increase in the concentration at noon (06:00 UTC) (Figure 10d). At the hot time of the day,
739 intense sunlight increased the light extinction by the particles. The DA system had to raise the
740 PM_{10} to fit the observed high AOD values. At dawn (00:00 UTC) or dusk (12:00 UTC), when
741 the sunlight was weak, the DA modifications were small, and the DA increases in the PM_{10}
742 fell to low levels. However, because the AOD constraint was only available in the daytime
743 and the AOD DA data were not always available as the data quality control (i.e., cloud
744 screening), assimilating AOD did not substantially increase the correlation of PM_x . The
745 analyzed PM_{10} in the DA experiments still had low correlations with the observed levels
746 ($R=0.33\text{--}0.35$).



747

748 **3.4 Assimilating Aerosol Scattering Coefficient**

749 Assimilating the aerosol scattering coefficient (DA_Esca) yielded overall analyses similar to
750 the phenomenon in DA_AOD. The aerosol scattering coefficient was reasonably good in the
751 analysis, with a monthly mean value of 244.6 Mm^{-1} and a high correlation of 0.97. The
752 analyzed monthly mean AOD was 0.57, better than the AOD of 0.31 when assimilating PM_x .
753 However, the surface particle concentrations were overestimated (i.e., positive biases by 32%
754 for $\text{PM}_{2.5}$, and 84% for PM_{10}), with a substantial increase in the coarse particle of OIN.
755 Overestimations appeared during the mild dust episodes (Figure 6b). This again indicated that
756 WRF-Chem underestimated the particle scattering efficiency, which was represented by the
757 ratio of the scattering coefficient to PM_{10} (Table 3). The DA system thus overfitted the PM_x
758 concentration to approach the observed scattering coefficient. The diurnal PM_{10} in the
759 analysis was similar to the assimilation of PM_x , showing a maximum improvement and a
760 robust nocturnal variation at 18:00 UTC. Assimilating the scattering coefficient failed to
761 improve the absorption coefficient. The monthly mean absorption coefficient was 19.1 Mm^{-1} ,
762 77% lower than the observed value.

763

764 **3.5 Assimilating Aerosol Absorption Coefficient**

765 In contrast to the above results, assimilating the absorption coefficient (DA_Eabs) degraded
766 all the analyses other than the absorption coefficient itself. The analyses showed substantial
767 daily variations, and strong positive biases appeared in the dust episodes (Figure 7). The
768 $\text{PM}_{2.5}$ was overestimated by a factor of four, and the PM_{10} was overestimated by a factor of
769 six. The increases occurred each hour and enlarged the diurnal variation of PM_{10} (Figure 10c).
770 The maximum increase in the mean value was at 06:00 UTC, also because of the strong
771 noontime heating in the model. As the particle concentration increased, the aerosol scattering
772 coefficient was overfitted to 849.0 Mm^{-1} , higher than the observed levels by a factor of four.
773 The monthly mean AOD was improbably up to 1.95. The improvement of the absorption
774 coefficient (which was 65.1 Mm^{-1}) was insufficient, and was 21% lower than the observed
775 levels.

776

777 Unlike DA_AOD and DA_Esca, assimilating the absorption coefficient cannot increase the
778 absorption data at the cost of PM_{10} overestimation. This DA failure in assimilating the
779 absorption coefficient indicates the model biases in the representation of the particle mixture
780 and the other absorbing particles (e.g., brown carbon and aged dust). With respect to the current
781 model, this failure is related to the aerosol absorption represented in WRF-Chem. The leading
782 absorption aerosol in WRF-Chem is BC. The BC particle in the second size ($0.156\text{--}0.625 \mu\text{m}$)
783 had the maximum absorption, according to Mie theory, and had the maximum DA
784 modifications in the second-size bin (Figure 11d). However, because the BC had a small
785 background concentration, the BC showed a small DA improvement and had small effects on
786 increasing the particle absorption. Meanwhile, the coarse dust particle concentration was
787 primarily increased, but the dust particles did not have a strong absorption as BC. As a result,
788 the model lowered the ratio of the absorption coefficient of PM_{10} by an order of magnitude
789 (Table 3). To fit the observed absorption coefficient, the DA system dramatically



790 overestimated the particle concentrations, aerosol scattering coefficient, and AOD, but the
791 analyzed absorption coefficient was still underestimated.

792

793 3.6 Assimilating Multi-source Observations

794 Assimilating an individual observation improves the corresponding model parameter (i.e.,
795 $PM_{2.5}$, PM_{10} , Esca, Eabs, and AOD) but may worsen other parameters. The reasons for the
796 inconsistent improvements are relevant to the aerosol model itself. These are: (1) the model
797 parameters have opposite signs in biases (e.g., one model parameter has a positive bias while
798 another has a negative bias); (2) the model biases have vast differences in magnitude (e.g., a
799 good fit of a parameter may lead to another's overfit) and the different biases in magnitude
800 cannot be reconciled through the adjoint operator because the forward operator is inaccurate
801 (e.g., lower particle extinction efficiency). Therefore, it may not always lead to a better
802 analysis when assimilating one type of observation. Simultaneous assimilation of the multi-
803 source observations imposes more definite constraints on the DA system and helps to
804 eliminate significant model biases.

805

806 In our case, simultaneous assimilation of the scattering and absorption coefficients
807 (DA_Esca_Eabs) resulted in the analyses when assimilating the scattering coefficient alone
808 (DA_Esca), and the inferior analysis in DA_Eabs vanished. This was because incorporating
809 the scattering coefficient constrained the aerosol number concentrations, which also benefited
810 from incorporating the observed absorption coefficient. Compared with the analysis
811 assimilating the PM_x alone (DA_ PM_x), assimilating the two aerosol attenuation coefficients
812 (DA_Esca_Eabs) better reproduced the AOD, but overestimated the surface particle
813 concentrations. In Figures 8–9, there were extremely high values on 28 April 2019, because
814 the scattering coefficient was missing at that time, during which the DA system assimilated
815 the absorption coefficient alone and worsened the analysis again. Simultaneous assimilation
816 of the surface particle concentration and the two aerosol attenuation coefficients
817 (DA_ PM_x _Esca_Eabs) improved these three assimilated parameters, but still gave a notable
818 low bias in AOD, 41% lower than the observed levels. Simultaneous assimilation of PM_x and
819 AOD (DA_ PM_x _AOD) gave the best overall DA results, in which all the analyses except the
820 absorption coefficient were not significantly different in the month mean values from the
821 observations. The analyses between DA_ PM_x _AOD and DA_ PM_x _Esca_Eabs were
822 comparable, except that the former additionally increased AOD better. Simultaneous
823 assimilation of all observations (DA_ PM_x _Esca_Eabs_AOD) did not substantially improve
824 the analyses when compared with DA_ PM_x _AOD because the surface coefficients, and AOD
825 had overlapped information of the light attenuation. A redundant information source did not
826 introduce extra constraints on the DA system. All the DA experiments failed to improve the
827 aerosol absorption coefficient, which always showed strong, low biases (> 76%) and low
828 correlations (< 0.5) in the analyses, implying room for improvement of our DA system.

829

Table 3, 4; Figure 6, 7, 8, 9, 10, 11

830

831 3.7 Vertical Profiles of Aerosol Concentrations



832 Figure 12 shows the vertical concentration profiles of $PM_{2.5}$ and PM_{10} . The DA system
833 increased the aerosol concentrations up to a height of 4 km, which is consistent with previous
834 studies on the Taklamakan Desert. Meng et al. (2019) simulated a deep dust layer thickness in
835 spring, with a depth of 3–5 km. Ge et al. (2014) analyzed the Cloud-Aerosol Lidar Orthogonal
836 Polarization data from 2006–2012 in the desert. They showed that dust could be lifted up to
837 5 km above the Tarim Basin, and even higher along the northern slope of the Tibetan Plateau.
838 Among our DA experiments, the analyzed PM_x in the lower atmosphere followed PM_x at the
839 surface. The vertical PM_{10} concentration increased quickly in the lowest three model layers
840 and maintained high values at heights of less than 3 km. This vertical profile corresponded
841 well to the background vertical error profile (Figure 3e), reflecting the deep dust transporting
842 layer. The $PM_{2.5}$ vertical profiles showed a rapid reduction with an increase in altitude. The
843 figure clearly shows that DA_ PM_x improved the PM_{10} better than $PM_{2.5}$, whereas DA_AOD
844 preferentially adjusted the coarse particles and overestimated the PM_{10} . DA_ PM_x _AOD
845 provided the best balance between the adjustments of $PM_{2.5}$ and PM_{10} .
846

Figure 12

847

848 4. Discussion

849 4.1 DA Impact on Aerosol Chemical Composition

850 The maximum concentrations of sulfate, ammonium, BC, and OC in April were 4.1, 1.5, 0.5,
851 and $1.3 \mu\text{g m}^{-3}$, respectively, in the background model data. Although a careful evaluation is
852 difficult because of the lack of aerosol chemical measurements, we speculated that the
853 aerosols (other than OIN) were considerably low. Anthropogenic emissions might be biased
854 for this city. The sources of emissions in residential/developing areas are principally
855 anthropogenic; yet the residential emission factor for the emission inventory compilation is
856 highly uncertain compared with the emission factors of power plants, industrial plants, and
857 vehicles (Li et al., 2017). Chlorine and sodium are selected to represent sea-salt aerosols in
858 WRF-Chem, yet the two concentrations were at very low concentrations in the model at
859 Kashi. This was despite the fact that the Taklamakan Desert had many atmospheric halite
860 particles, which were Cl- and Na-rich and accounted for 10% of the total particles in the
861 desert (Okada and Kai, 2004).

862

863 For control variable design, our DA system modifies the chemical composition of each
864 aerosol according to the BEC values. However, all the DA experiments showed that the PM_{10}
865 chemical fractions remain close to their background values (Figure 13). The low biases cannot
866 be improved via DA because the aerosol chemical measurements were not available. In
867 addition, the differences between DA_Esca and DA_Esca_Eabs were quite small (Figure 13c,
868 e), indicating that assimilating the aerosol absorption coefficient did not enhance particle
869 absorption (19.1^{-1} vs. 20.0 Mm^{-1} in Table 3) in our system. The assimilation of the aerosol
870 absorption coefficient alone (DA_Eabs) increased the percentage of BC to 7.1%, which was
871 slightly higher than the 6.5% background BC. The first reason for the small changes in the
872 aerosol chemical proportions is that the scattering aerosols (i.e., sulfate, nitrate, and
873 ammonium), use the same refractive index and hygroscopicity parameter in WRF-Chem.
874 Therefore, the AOD had virtually the same sensitivity to composition of each aerosol, and



875 assigned comparable modification to each composition. When assimilating the total quantities
876 of aerosols (e.g., $PM_{2.5}$, PM_{10} , and AOD), it is difficult to distinguish different aerosol
877 chemical contributions. Secondly, DA_Eabs increased the aerosol number concentration;
878 meanwhile, the rising number concentration increased the scattering aerosols, which
879 prevented a substantial rise in the BC fraction. Third, the concentrations of anthropogenic
880 aerosols were lower than anticipated. They had comparable low background errors and could
881 not be distinguished because of their small differences in BEC values. Overall, it seems that
882 differences in aerosol chemical composition from assimilating the aerosol optical data are
883 smaller than the difference in model setting (e.g., using other aerosol chemistry mechanisms,
884 or using finer aerosol size bins). The assimilation of the total aerosol quantities cannot
885 eliminate the intrinsic bias in aerosol composition. Thus, accurate aerosol chemistry and
886 optical modules are crucial to attain a better background aerosol chemical data for DA
887 analysis (Saide et al., 2020).
888

Figure 13

889

890 4.2 DA Impact on Aerosol Direct Radiative Forcing

891 Table 4 shows the instantaneous clear-sky ADRF in the background data and the analyses of
892 DA_{PM_x} and $DA_{PM_x_AOD}$. After the analyses, the DA effect (various DA frequencies for
893 assimilating AOD and the surface particle concentrations) gradually faded away after
894 restarting the model run. We therefore focused on the instantaneous radiative forcing values
895 one hour after assimilating AOD data. This ensured that the comparison was based on similar
896 analysis times and showed effective DA effects. As the dust was the predominant component,
897 the ADRF in this section was closely equivalent to the dust radiative forcing.

898

899 Dust redistributes the energy between the land and the atmosphere. The atmosphere gains
900 more shortwave energy as the dust particle absorption; the warming atmosphere also emits
901 more longwave energy as it absorbs shortwave energy. The change in energy budget at the
902 surface is correspondingly the opposite of that in the atmosphere. As shown in Table 4, the
903 enhancements in surface cooling forces were slightly stronger than the atmospheric warming
904 forcings. The differences between the surface forcing and atmospheric forcing indicate the
905 ADRF at the top of the atmosphere (TOA). The TOA ADRF when assimilating the surface
906 particle concentrations was enhanced by 12% in the shortwave, 83% in the longwave, and 6%
907 in the net forcing values, and enhanced by 40%, 55%, and 38%, respectively, when
908 assimilating the AOD. Apparently, assimilating PM_x alone is not sufficient to accurately
909 estimate the ADRF value. At Kashi, the total net clear-sky ADRF with assimilating surface
910 particles and AOD were -10.5 Wm^{-2} at the TOA, $+19.5 \text{ Wm}^{-2}$ within the atmosphere, and $-$
911 30.0 Wm^{-2} at the surface, respectively, enhanced by 46%, 153%, and 100% respectively,
912 compared to the background ADRF values. Because the AOD observation is only
913 sporadically available because of cloud screening in retrieval data, the DA experiments still
914 cannot eliminate the low bias in AOD in WRF-Chem. The ADRF values in the DA
915 experiments are still likely to be lower than the plausible aerosol radiative forcing at Kashi.

916

917 5. Conclusions



918 This study described our revised GSI DA system for assimilating aerosol observed data for
919 the four-size bin sectional MOSAIC aerosol mechanism in WRF-Chem. The DA system has
920 new design adjoint operators for the multi-wavelength AOD, aerosol scattering, and
921 absorption coefficients measured by the sun-sky radiometer, nephelometer, and aethalometer,
922 respectively. We examined the DA system for Kashi city in northwestern China by
923 assimilating the multi-wavelength aerosol optical measurements gathered by the Dust Aerosol
924 Observation–Kashi field campaign of April 2019 and the concurrent hourly measurements of
925 surface $PM_{2.5}$ and PM_{10} concentrations from the local environmental monitoring sites.

926
927 Our DA system includes two main aspects. Firstly, the control variable is the aerosol chemical
928 composition per size bin corresponding to the WRF-Chem output data. This design allows the
929 modification of the composition of each aerosol, based on their background error covariances.
930 The number of control variables could be reduced by intentionally excluding a few aerosol
931 compositions in a specific case, if these compositions had low concentrations. Second, the DA
932 system incorporates the observed AOD by assimilating the column mean aerosol extinction
933 coefficient. This transfer avoids handling sensitivity from light attenuation length to the
934 aerosol mass concentration in the adjoint operator, which is difficult to accurately estimate
935 and introduces significant errors in the operator. The adjoint operator for AOD has two
936 variants that incorporate nephelometer and aethalometer measurements.

937
938 The most abundant aerosol at Kashi in April 2019 was dust. The WRF-Chem model captured
939 the main dust episodes, but only simulated half the monthly mean concentrations of $PM_{2.5}$ and
940 PM_{10} . Furthermore, the model failed to capture the peak concentrations from a dust storm on
941 24 April. The aerosol scattering/absorption coefficients and AOD in the background data
942 showed strong low biases and weak correlations with the observed levels. The DA systems
943 did, however, effectively assimilate the surface particle concentrations, aerosol scattering
944 coefficients, and AOD. Some deficiencies in the DA analysis were related to the forward
945 model bias in transferring the aerosol mass concentrations to the aerosol optical parameter.
946 Simultaneous assimilation of the $PM_{2.5}$ and PM_{10} concentrations improved the model aerosol
947 concentrations, with significant increases in the coarse particles; meanwhile, the analyzed
948 AOD was 56% lower than observed levels. The assimilation of AOD significantly improved
949 the AOD but overestimated the surface PM_{10} concentration by a factor of at least two.
950 Assimilating the aerosol scattering coefficient improved the scattering coefficient in the
951 analysis but overestimated the surface PM_{10} concentration by 84%. It therefore seems that
952 WRF-Chem underestimated the particle extinction efficiency. As a compensation, the DA
953 system overestimated the aerosol concentration to fit the observed optical values, yielding
954 overly high particle concentrations.

955
956 A notable problem was the assimilation of the absorption coefficient, which greatly
957 overestimated the monthly mean values by a factor of at least four in the model parameters
958 and yielded overly strong daily variations for the parameters. The aerosol absorption
959 coefficient was improved but was still 21% lower than observed values. This defect was also
960 apparent in the low particle absorption efficiency of WRF-Chem. The biases of the model in
961 aerosol particle mixture and aged dust as well as the “missing” absorption of brown carbon,



962 accounted for the bias in absorption efficiency, which would have worsened the DA analysis
963 when assimilating the absorption coefficient.
964
965 Simultaneous assimilation of the multi-source observations imposes a more definite constraint
966 and helps improve model parameters. Simultaneously assimilating the scattering and
967 absorption coefficients eliminated the defect of assimilating the absorption coefficient. It also
968 provided comparable improvements for assimilating the surface particles and AOD; the latter
969 additionally improved the AOD analysis. The most effective DA is the simultaneous
970 assimilation of surface particle concentration and AOD, which provides the best overall DA
971 analysis.
972
973 Our design of control variables allowed the DA system to adjust the aerosol chemical
974 compositions individually. However, the analyzed anthropogenic aerosol chemical fractions
975 were almost equivalent to the background chemical fractions. The reason is that the
976 hydrophilic aerosols have equivalent or comparable refractive indices and hygroscopic
977 parameters in the forward operator; they therefore have comparable adjoint operator values
978 when assimilating the aerosol optical data. It may be possible to separate the chemical
979 compositions based on their background errors. In our case, the anthropogenic aerosols were
980 unrealistically low at Kashi, probably owing to the low biases in the anthropogenic emissions.
981 The low background concentrations led to low background errors and hence few increments
982 for all chemical compositions. As a result, the chemical fractions of the anthropogenic
983 aerosols remained close to their background values.
984
985 When assimilating surface particles and AOD, the instantaneous clear-sky ADRF at Kashi
986 were -10.5 Wm^{-2} at the TOA, $+19.5 \text{ Wm}^{-2}$ within the atmosphere, and -30.0 Wm^{-2} at the
987 surface, respectively. Since the DA analyses still lowered the AOD value, the aerosol
988 radiative forcing values assimilating the observations were also underestimated.
989
990 The limitations that necessitate further research include:
991 (1) The binning strategy. The desired strategy should link the circulation flow and
992 particle emission sources. A better hybrid DA coupled with the ensemble Kalman filter will
993 be more effective for estimating the aerosol background error.
994 (2) The observational error. This could be elaborated further. The PM_{10} included the
995 anthropogenic coarse particles, which should be separated from the dust originating from the
996 desert (Jin et al., 2019). We set the observation errors for PM_x and AOD to the conventional
997 values. The observational errors of the nephelometer and aethalometer were slightly arbitrary
998 in this study, necessitating further consideration.
999 (3) The adjoint operator. This needs to be modified to assimilate the aerosol absorption
1000 coefficient or absorption AOD.
1001 (4) The DA system. Our revised DA system was based on four-size bin MOSAIC
1002 aerosols, but it can be extended to work with eight-size bin MOSAIC aerosols in WRF-Chem.
1003 When assimilating aerosol optical data, the DA quality is strongly dependent on the forward
1004 model. The responses of our DA analysis to the bias and uncertainty in the forward aerosol
1005 optical model in WRF-Chem thus need further investigation.



1006 **Author contributions**

1007 WC developed the DA system, performed the analyses and wrote the paper. ZL led the field
1008 campaign and revised the paper. YZ and KL implemented the observations and the data
1009 quality control. YZ helped to design the new adjoint operator. JC verified the DA system.

1010

1011 **Competing interests**

1012 The authors declare that they have no conflict of interest.

1013

1014 **Code/Data availability**

1015 The official GSI code is available at [https://dtcenter.org/community-code/gridpoint-statistical-](https://dtcenter.org/community-code/gridpoint-statistical-interpolation-gsi/download)
1016 [interpolation-gsi/download](https://dtcenter.org/community-code/gridpoint-statistical-interpolation-gsi/download). The aerosol measurements at Kashi belong to the Sun-sky
1017 radiometer Observation NETwork (SONET) which is accessible at
1018 <http://www.sonet.ac.cn/en/index.php>.

1019

1020 **Acknowledgments**

1021 This work is supported by the National Key Research and Development Program of China
1022 (Grant number 2016YFE0201400).

1023

1024 **References**

- 1025 Bannister, R. N.: A review of operational methods of variational and ensemble-variational
1026 data assimilation, *Q.J.R. Meteorol. Soc.*, 143, 607-633, doi:10.1002/qj.2982, 2017.
- 1027
- 1028 Bao, Y., Zhu, L., Guan, Q., Guan, Y., Lu, Q., Petropoulos, G. P., Che H., Ali, g., Dong, Y.,
1029 Tang, Z., Gu, Y., Tang, W., and Hou, Y.: Assessing the impact of Chinese FY-3/MERSI
1030 AOD data assimilation on air quality forecasts: sand dust events in northeast China, *Atmos.*
1031 *Environ.*, 205, 78-89, doi:10.1016/j.atmosenv.2019.02.026, 2019.
- 1032
- 1033 Calil, P. H. R., Doney, S. C., Yumimoto, K., Eguchi, K., and Takemura, T.: Episodic
1034 upwelling and dust deposition as bloom triggers in low-nutrient, low-chlorophyll regions, *J.*
1035 *Geophys. Res.*, 116, C06030, doi:10.1029/2010jc006704, 2011.
- 1036
- 1037 Chen, D., Liu, Z., Schwartz, C. S., Lin, H.-C., Cetola, J. D., Gu, Y., and Xue, L.: The impact
1038 of aerosol optical depth assimilation on aerosol forecasts and radiative effects during a wild
1039 fire event over the United States, *Geosci. Model Dev.*, 7, 2709-2715, doi:10.5194/gmd-7-
1040 2709-2014, 2014.
- 1041
- 1042 Chen, L., Gao, Y., Zhang, M., Fu, J. S., Zhu, J., Liao, H., Li, J., Huang, K., Ge, B., Wang, X.,
1043 Lam, Y. F., Lin, C.-Y., Itahashi, S., Nagashima, T., Kajino, M., Yamaji, K., Wang, Z., and
1044 Kurokawa, J.-i.: MICS-Asia III: multi-model comparison and evaluation of aerosol over East
1045 Asia, *Atmos. Chem. Phys.*, 19, 11911-11937, doi:10.5194/acp-19-11911-2019, 2019.
- 1046
- 1047 Chen, S.-H., and Sun, W.-Y.: A one-dimensional time dependent cloud model, *J. Meteor. Soc.*
1048 *Japan*, 80, 1, 99-118, doi:10.2151/jmsj.80.99, 2002.
- 1049



- 1050 Cheng, X., Liu, Y., Xu, X., You, W., Zang, Z., Gao, L., Chen, Y., Su, D., and Yan, P.: Lidar
1051 data assimilation method based on CRTM and WRF-Chem models and its application in
1052 PM_{2.5} forecasts in Beijing, *Sci. Total Environ.*, 682, 541-552,
1053 doi:10.1016/j.scitotenv.2019.05.186, 2019.
- 1054
1055 Descombes, G., Auligné, T., Vandenberghe, F., Barker, D. M., and Barré, J.: Generalized
1056 background error covariance matrix model (GEN_BE v2.0), *Geosci. Model Dev.*, 8, 669-696,
1057 doi:10.5194/gdm-8-669-2015, 2015.
- 1058
1059 Fan, J., Shang, Y., Chen, Q., Wang, S., Zhang, X., Zhang, L., Zhang, Y., Xu, X., and Jiang,
1060 P.: Investigation of the “dust reservoir effect” of the Tarim Basin using WRF-GOCART
1061 model, *Arab. J. Geosci.*, 13, 214, doi:10.1007/s12517-020-5154-x, 2020.
- 1062
1063 Fast, J. D., Gustafson, W. I., Easter, R. C., Zaveri, R. A., Barnard, J. C., Chapman, E. G.,
1064 Grell, G. A. Peckham, S. E.: Evolution of ozone, particulates, and aerosol direct radiative
1065 forcing in the vicinity of Houston using a fully coupled meteorology-chemistry-aerosol
1066 model, *J. Geophys. Res.-Atmos.*, 111, D21305, doi:10.1029/2005jd006721, 2006.
- 1067
1068 Feng, S., Jiang, F., Jiang, Z., Wang, H., Cai, Z., and Zhang, L.: Impact of 3DVAR
1069 assimilation of surface PM_{2.5} observations on PM_{2.5} forecasts over China during wintertime,
1070 *Atmos. Environ.*, 187, 34-49, doi:10.1016/j.atmosenv.2018.05.049, 2018.
- 1071
1072 Ge, J. M., Huang, J. P., Xu, C. P., Qi, Y. L., and Liu, H. Y.: Characteristics of Taklimakan
1073 dust emission and distribution: A satellite and reanalysis field perspective, *J Geophys. Res.*
1074 *Atmos.*, 119, 11772-11783, doi:10.1002/2014jd022280, 2014.
- 1075
1076 Ge, J. M., Liu, H., Huang, J., and Fu, Q.: Taklimakan desert nocturnal low-level jet:
1077 climatology and dust activity, *Atmos. Chem. Phys.*, 16, 7773-7783, doi:10.5194/acp-16-7773-
1078 2016, 2016.
- 1079
1080 Ginoux, P., Chin, M., Tegen, I., Prospero, J. M., Holben, B., Dubovik, O., and Lin, S.-J.:
1081 Sources and distributions of dust aerosols simulated with the GOCART model, *J. Geophys.*
1082 *Res.*, 106, D17, 20255-20273, doi: 10.1029/2000JD000053, 2001.
- 1083
1084 Giorgi, F., and Mearns, L. O.: Introduction to special section: Regional climate modeling
1085 revisited, *J. Geophys. Res.*, 104, D6, 6335-6352, doi:10.1029/98JD02072, 1999.
- 1086
1087 Grell, G. A., Peckham, S. E., Schmitz, R., McKeen, S. A., Frost, G., Skamarock, W. C., and
1088 Eder, B.: Fully coupled “online” chemistry within the WRF model. *Atmos. Environ.*, 39,
1089 6957-7975, doi:10.1016/j.atmosenv.2005.04.027, 2005.
- 1090
1091 Guenther, A., Karl, T., Harley, P., Wiedinmyer, C., Palmer, P. I., and Geron, C.: Estimates of
1092 global terrestrial isoprene emissions using MEGAN (Model of Emissions of Gases and



- 1093 Aerosols from Nature), *Atmos. Chem. Phys.*, 6, 3181-3210, doi:10.5194/acp-6-3181-2006,
1094 2006.
1095
- 1096 He, J., Zhang, Y., Wang, K., Chen, Y., Leung, L. R., Fan, J., Li, M., Zheng, B., Zhang, Q.,
1097 Duan, F., and He, K.: Multi-year application of WRF-CAM5 over East Asia-Part I:
1098 Comprehensive evaluation and formation regimes of O₃ and PM_{2.5}, *Atmos. Environ.*, 165,
1099 122-142, doi:10.1016/j.atmosenv.2017.06.015, 2017.
1100
- 1101 Hong, S.-Y., Noh, Y., Dudhia, J.: A new vertical diffusion package with an explicit treatment
1102 of entrainment processes, *Mon. Wea. Res.*, 134, 2318-2341, doi:10.1175/MWR3199.1, 2006.
1103
- 1104 Huang, J., Wang, T., Wang, W., Li, Z., and Yan, H.: Climate effects of dust aerosols over
1105 East Asian arid and semiarid regions, *J. Geophys. Res.*, 119, 11398-11416,
1106 doi:10.1002/2014jd021796, 2014.
1107
- 1108 Hong, J., Mao, F., Min, Q., Pan, Z., Wang, W., Zhang, T., and Gong, W.: Improved PM_{2.5}
1109 predictions of WRF-Chem via the integration of Himawari-8 satellite data and ground
1110 observations, *Environ. Pollut.*, 263, 114451, doi:10.1016/j.envpol.2020.114451, 2020.
1111
- 1112 Iacono, M. J., Delamere, J. S., Mlawer, E. J., Shephard, M. W., Clough, S. A., and Collins,
1113 W. D.: Radiative forcing by long-lived greenhouse gases: Calculations with the AER radiative
1114 transfer models, *J. Geophys. Res.*, 113, D13103, doi:10.1029/2008JD009944, 2008.
1115
- 1116 Jia, R., Liu, Y., Chen, B., Zhang, Z., and Huang, J.: Source and transportation of summer dust
1117 over the Tibetan Plateau, *Atmos. Environ.*, 123, 210-219,
1118 doi:10.1016/j.atmosenv.2015.10.038, 2015.
1119
- 1120 Jiang, Z., Liu, Z., Wang, T., Schwartz, C. S., Lin, H.-C., and Jiang, F.: Probing into the
1121 impact of 3DVAR assimilation of surface PM₁₀ observations over China using process
1122 analysis, *J. Geophys. Res.*, 118, 6738-6749, doi:10.1002/jgrd.50495, 2013.
1123
- 1124 Jin, J., Lin, H. X., Segers, A., Xie, Y., and Heemink, A.: Machine learning for observation
1125 bias correction with application to dust storm data assimilation, *Atmos. Chem. Phys.*, 19,
1126 10009-10026, doi:10.5194/acp-19-10009-2019.
1127
- 1128 Li, L., Li, Z., Chang, W., Ou, Y., Goloub, P., Li, C., Li, K., Hu, Q., Wang, J., and Wendisch,
1129 M.: Solar radiative forcing of aerosol particles near the Taklimakan desert during the Dust
1130 Aerosol Observation-Kashi campaign in Spring 2019, *Atmos. Chem. Phys. Discuss.*,
1131 doi:10.5194/acp-2020-60, in review, 2020.
1132
- 1133 Li, M., Liu, H., Geng, G., Hong, C., Liu, F., Song, Y., Tong, D., Zheng, B., Cui, H., Man, H.,
1134 Zhang, Q., and He, K.: Anthropogenic emission inventories in China: a review, *Natl. Sci.*
1135 *Rev.*, 4, 834-866, doi:10.1093/nsr/nwx150, 2017.
1136



- 1137 Liu, Z., Liu, Q., Lin, H.-C., Schwartz, C. S., Lee, Y.-H., and Wang, T.: Three-dimensional
1138 variational assimilation of MODIS aerosol optical depth: Implementation and application to a
1139 dust storm over East Asia, *J. Geophys. Res.*, 116, D23206, doi:10.1029/2011JD016159, 2011.
1140
- 1141 Li, Z., Zang, Z., Li, Q. B., Chao, Y., Chen, D., Ye, Z., Liu, Y., and Liou, K. N.: A three-
1142 dimensional variational data assimilation system for multiple aerosol species with
1143 WRF/Chem and an application to PM_{2.5} prediction, *Atmos. Chem. Phys.*, 13, 4265-4278,
1144 doi:10.5194/acp-13-4265-2013, 2013.
1145
- 1146 Ma, C., Wang, T., Mizzi, A. P., Anderson, J. L., Zhuang, B., Xie, M., and Wu, R.:
1147 Multiconstituent data assimilation with WRF-Chem/DART: Potential for adjusting
1148 anthropogenic emissions and improving air quality forecasts over eastern China, *J. Geophys.*
1149 *Res. Atmos.*, 124, 7393-7412, doi:10.1029/2019JD030421, 2019.
1150
- 1151 Ma, C., Wang, T., Jiang, Z., Wu, H., Zhao, M., Zhuang, B., Li, S., Xie, M., Li, M., Liu, J.,
1152 and Wu, R.: Importance of bias correction in data assimilation of multiple observations over
1153 eastern China using WRF-Chem/DART, *J. Geophys. Res. Atmos.*, 125, e2019JD031465,
1154 doi:10.1029/2019JD031465, 2020.
1155
- 1156 Massart, S., Pajot, B., Piacentini, A., and Pannekoucke, O.: On the merits of using a 3D-
1157 FGAT assimilation scheme with an outer loop for atmospheric situations governed by
1158 transport, *Mon. Weather Rev.*, 138, 12, 4509-4522, doi:10.1175/2010MWR3237.1, 2010.
1159
- 1160 Meng, L., Yang, X., Zhao, T., He, Q., Lu, H., Mantimin, A., Huo, W., Yang, F., and Liu, C.:
1161 Modeling study on three-dimensional distribution of dust aerosols during a dust storm over
1162 the Tarim Basin, Northwest China, *Atmos. Res.*, 218, 285-295,
1163 doi:10.1016/j.atmosres.2018.12.006, 2019.
1164
- 1165 Okada, K., and Kai, K.: Atmospheric mineral particles collected at Qira in the Taklamakan
1166 Desert, China, *Atmos. Environ.*, 38, 6927-6935, doi:10.1016/j.atmosenv.2004.03.078, 2004.
1167
- 1168 Pagowski, M., Grell, G. A., McKeen, S. A., Peckham, S. E., and Devenyi, D.: Three-
1169 dimensional variational data assimilation of ozone and fine particulate matter observations:
1170 some results using the Weather Research and Forecasting – Chemistry model and Grid-point
1171 Statistical Interpolation, *Q. J. R., Meteorol. Soc.*, 136, 2014-2024, doi:10.1002/qj.700, 2010.
1172
- 1173 Pagowski, M., Liu, Z., Grell, G. A., Hu, M., Lin, H.-C., and Schwartz, C. S.: Implementation
1174 of aerosol assimilation in Gridpoint Statistical Interpolation (v.3.2) and WRF-Chem (v.3.4.1),
1175 *Geosci. Model Dev.*, 7, 1621-1627, doi:10.5194/gmd-7-1621-2014, 2014.
1176
- 1177 Pang, J., Liu, Z., Wang, X., Bresch, J., Ban, J., Chen, D., and Kim, J.: Assimilating AOD
1178 retrievals from GOCI and VIIRS to forecast surface PM_{2.5} episodes over eastern China,
1179 *Atmos. Environ.*, 179, 288-304, doi:10.1016/j.atmosenv.2018.02.011, 2018.
1180



- 1181 Pang, J., Wang, X., Shao, M., Chen, W., and Chang, M.: Aerosol optical depth assimilation for
1182 a modal aerosol model: Implementation and application in AOD forecasts over East Asia, *Sci.*
1183 *Total Environ.*, 719, 137430, doi:10.1016/j.scitotenv.2020.137430, 2020.
1184
- 1185 Parrish, D. F., and Derber, J. C.: The National Meteorological Center's spectral statistical-
1186 interpolation analysis system, *Mon. Weather Rev.*, 120, 1747-1763, doi: 10.1175/1520-
1187 0493(1992)120<1747:TNMCSS>2.0.CO;2, 1992.
1188
- 1189 Peng, Z., Liu, Z., Chen, D., and Ban, J.: Improving PM_{2.5} forecast over China by the joint
1190 adjustment of initial conditions and source emissions with an ensemble Kalman filter, *Atmos.*
1191 *Chem. Phys.*, 17, 4837-4855, doi:10.5194/acp-17-4837-2017, 2017.
1192
- 1193 Peng, Z., Lei, L., Liu, Z., Sun, J., Ding, A., Ban, J., Chen, D., Kou, X., and Chu, K.: The
1194 impact of multi-species surface chemical observation assimilation on air quality forecasts in
1195 China, *Atmos. Chem. Phys.*, 18, 17387-17404, doi:10.5194/acp-18-17387-2018, 2018.
1196
- 1197 Purser, R. J., Wu, W.-S., Parrish, D. F., and Roberts, N. M.: Numerical aspects of the
1198 application of recursive filters to variational statistical analysis. Part I: spatially homogeneous
1199 and isotropic gaussian covariances, *Mon. Weather Rev.*, 131, 1524-1535, doi: 10.1175//1520-
1200 0493(2003)131<1524:NAOTAO>2.0.CO;2, 2003a.
1201
- 1202 Purser, R. J., Wu, W.-S., Parrish, D. F., and Roberts, N. M.: Numerical aspects of the
1203 application of recursive filters to variational statistical analysis. Part II: spatially
1204 inhomogeneous and anisotropic general covariances, *Mon. Weather Rev.*, 131, 1536-1548,
1205 doi: 10.1175//2543.1, 2003b.
1206
- 1207 Saide, P. E., Carmichael, G. R., Liu, Z., Schwartz, C. S., Lin, H. C., da Silva, A. M., and
1208 Hyer, E.: Aerosol optical depth assimilation for a size-resolved sectional model: impacts of
1209 observationally constrained, multi-wavelength and fine mode retrievals on regional scale
1210 analyses and forecasts, *Atmos. Chem. Phys.*, 13, 10425-10444, doi:10.5194/acp-13-10425-
1211 2013, 2013.
1212
- 1213 Saide, P. E., Kim, J., Song, C. H., Choi, M., Cheng, Y., and Carmichael, G. R.: Assimilation
1214 of next generation geostationary aerosol optical depth retrievals to improve air quality
1215 simulations, *Geophys. Res. Lett.*, 41, 9188-9196, doi:10.1002/2014GL062089, 2014.
1216
- 1217 Saide, P. E., Gao, M., Lu, Z., Goldberg, D., Streets, D. G., Woo, J.-H., Beyersdorf, A., Corr,
1218 C. A., Thornhill, K. L., Anderson, B., Hair, J. W., Nehrir, A. R., Diskin, G. S., Jimenez, J. L.,
1219 Nault, B. A., Campuzano-Jost, P., Dibb, J., Heim, E., Lamb, K. D., Schwarz, J. P., Perring,
1220 A. E., Kim, J., Choi, M., Holben, B., Pfister, G., Hodzic, A., Carmichael, G. R., Emmons, L.,
1221 and Crawford, J. H.: Understanding and improving model representation of aerosol optical
1222 properties for a Chinese haze event measured during KORUS-AQ, *Atmos. Chem. Phys.*, 20,
1223 6455-6478, doi:10.5194/acp-20-6455-2020, 2020.
1224



- 1225 Schwartz, C. S., Liu, Z., Lin, H.-C., and McKeen, S. A.: Simultaneous three-dimensional
1226 variational assimilation of surface fine particulate patten and MODIS aerosol optical depth, J.
1227 Geophys. Res., 117, D13202, doi:10.1029/2011JD017383, 2012.
1228
- 1229 Sič, B., Amraoui, L. E., Piacentini, A., Marécal, V., Emili, E., Cariolle, D., Prather, M., and
1230 Attié, J.-L.: Aerosol data assimilation in the chemical transport model MOCAGE during the
1231 TRAQA/ChArMEx campaign: aerosol optical depth, Atmos. Chem. Phys., 9, 5535-5554,
1232 doi:10.5194/amt-9-5535-2016, 2016.
1233
- 1234 Tang, Y., Pagowski, M., Chai, T., Pan, L., Lee, P., Baker, B., Kumar, R., Monache, L. D.,
1235 Tong, D., and Kim, H.-C.: A case study of aerosol data assimilation with the Community
1236 Multi-scale Air Quality Model over the contiguous United States using 3D-Var and optimal
1237 interpolation methods, Geosci. Model Dev., 10, 4743-4758, doi:10.5194/gmd-10-4743-2017,
1238 2017.
1239
- 1240 Tewari, M., Chen, F., Wang, W., Dudhai, J., LeMone, M. A., Mitchell, K., Ek, M., Gayno,
1241 G., Wegiel, J., and Cuenca, R. H.: Implementation and verification of the unified NOAA land
1242 surface model in the WRF model. 20th conference on weather analysis and forecasting/16th
1243 conference on numerical weather prediction, pp. 11-15.
1244
- 1245 Wang, K.-Y., Lary, D. J., Shallcross D. E., Hall, S. M., and Pyle, J. A.: A review on the use of
1246 the adjoint method in four-dimensional atmospheric-chemistry data assimilation, Q. J. R.
1247 Meteorol. Soc., 127, 2181-2204, doi:10.1002/qj.49712757616, 2001.
1248
- 1249 Wu, W.-S., Purser, r. J., and Parrish, D. F.: three-dimensional variational analysis with
1250 spatially inhomogeneous covariances, Mon. Weather Rev., 130, 12, 2905-2916,
1251 doi: 10.1175/1520-0493(2002)130<2905:TDVAWS>2.0.CO;2, 2002.
1252
- 1253 Xia, X., Min, J., Shen, F., Wang, Y., and Yang, C.: Aerosol data assimilation using data from
1254 Fengyun-3A and MODIS: application to a dust storm over East Asia in 2011, Adv. Atmos.
1255 Sci., 36, 1-14, doi:10.1007/s00376-018-8075-9, 2019a.
1256
- 1257 Xia, X., Min, J., Wang, Y., Shen, F., Yang, C., and Sun, Z.: Assimilating Himawari-8 AHI
1258 aerosol observations with a rapid-update data assimilation system, Atmos. Environ., 215,
1259 116866, doi:10.1016/j.atmosenv.2019.116866, 2019b.
1260
- 1261 Zang, Z., Li, Z., Pan, X., Hao, Z., and You, W.: Aerosol data assimilation and forecasting
1262 experiments using aircraft and surface observations during CalNex, Tellus B., 68,1, 29812,
1263 doi:10.3402/tellusb.v68.29812, 2016.
1264
- 1265 Zaveri, R. A., and Peters, L. K.: A new lumped structure photochemical mechanism for large-
1266 scale applications, J. Geophys. Res., 104, 30387-30415, doi:10.1029/1999JD900876, 1999.
1267



- 1268 Zaveri, R. A., Easter, R. C., Fast, J. D., Peters, L. K.: Model for simulating aerosol
1269 interactions and chemistry (MOSAIC), *J. Geophys. Res.*, 113, D13204,
1270 doi:10.1029/2007JD008782, 2008.
1271
- 1272 Zhao, J., Ma, X., Wu, S., and Sha, T.: Dust emission and transport in Northwest China: WRF-
1273 Chem simulation and comparisons with multi-sensor observation, *Atmos. Res.*, 241, 104978,
1274 doi:10.1016/j.atmosres.2020.104978, 2020.

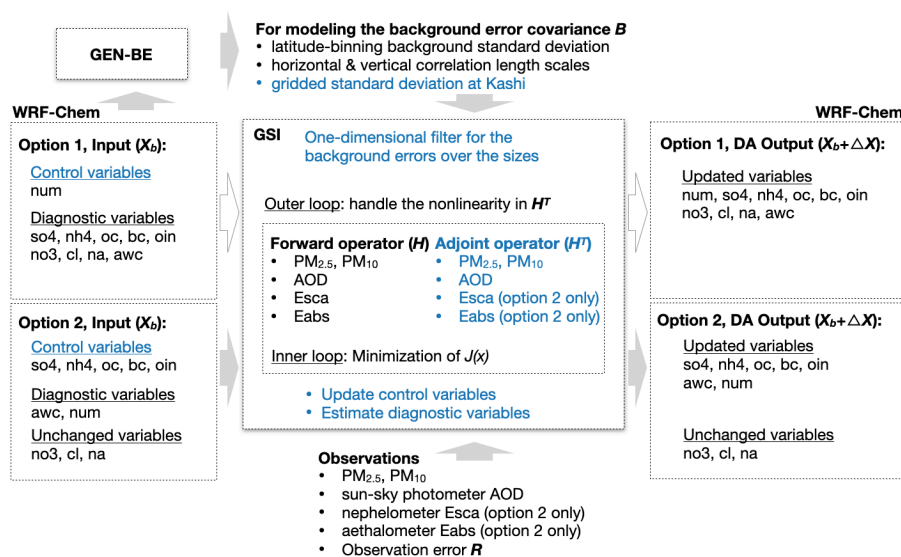


Figure 1. The workflow of aerosol DA in the revised GSI system for the sectional MOSAIC aerosols in WRF-Chem. The contents in blue are the portions we developed. The arrows in gray indicate the workflow of option 2 that we did in this study. Only option 2 can assimilate the aerosol scattering/absorption coefficients. Abbreviations: so4, sulfate; nh4, ammonium; oc, organic carbon; bc, black carbon; oin, other inorganic matter; awc, aerosol water content; num, aerosol number concentration; no3, nitrate; cl, chlorine; na, sodium; Esca, aerosol scattering coefficient; Eabs, aerosol absorption coefficient.

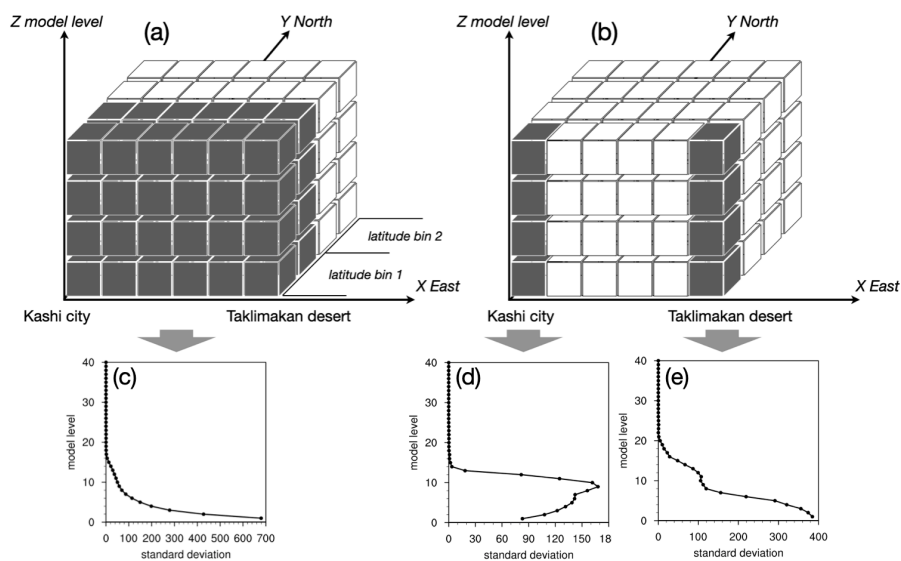


Figure 2. Schematic diagram of the binning strategy for modeling background error covariance matrix on (a) the latitude binning data or (b) the gridded data; and the vertical profiles of standard deviations ($\mu\text{g kg}^{-1}$) of the coarse OIN component concentration at 06:00UTC in April 2019 (c) on average over the latitude bins, (d) at Kashi city grid and (e) at the Taklimakan desert grid (i.e., 1.5 degrees east to the Kashi city).

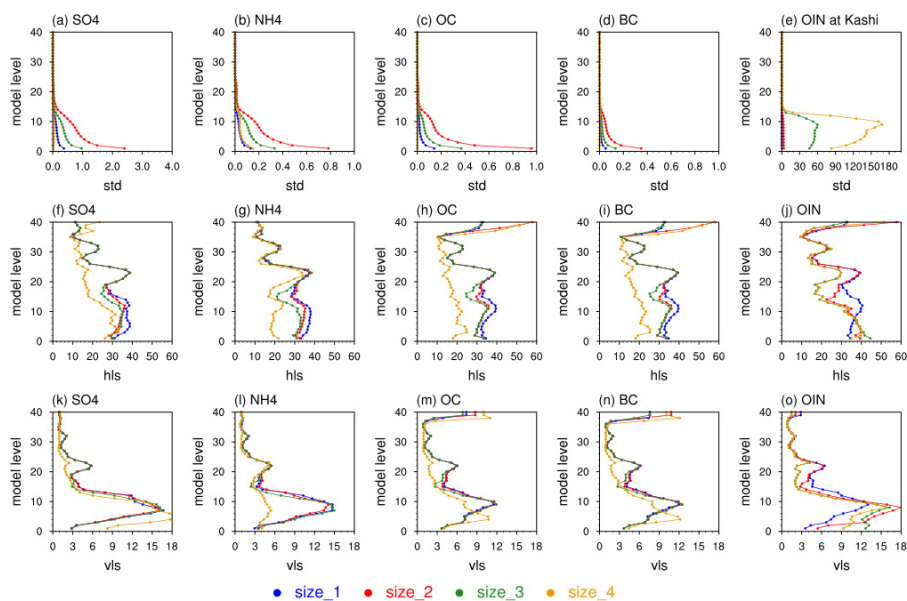


Figure 3. Background error standard deviations (std, a-e, $\mu\text{g kg}^{-1}$), horizontal correlation length scales (hls, f-j, km), and vertical correlation length scales (vls, k-o, km) at 00:00 UTC in April 2019 for the sectional sulfate, ammonium, organic aerosol (OC), black carbon (BC), and other inorganic aerosols (OIN, including dust) in the model domain 2. All the quantities in figures were the averages over the latitude bins with a half degree width, except that figure (e) represented the standard deviation of OIN at the Kashi grid.

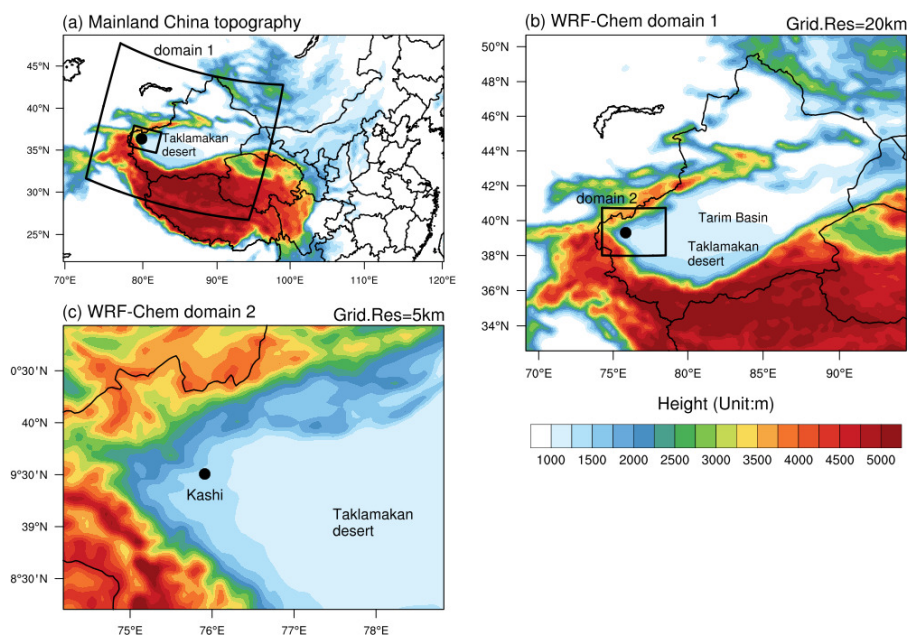


Figure 4. Topography in China (a) and the model domains with the grid resolution of 20 km (b) and 5 km (c) in WRF-Chem.

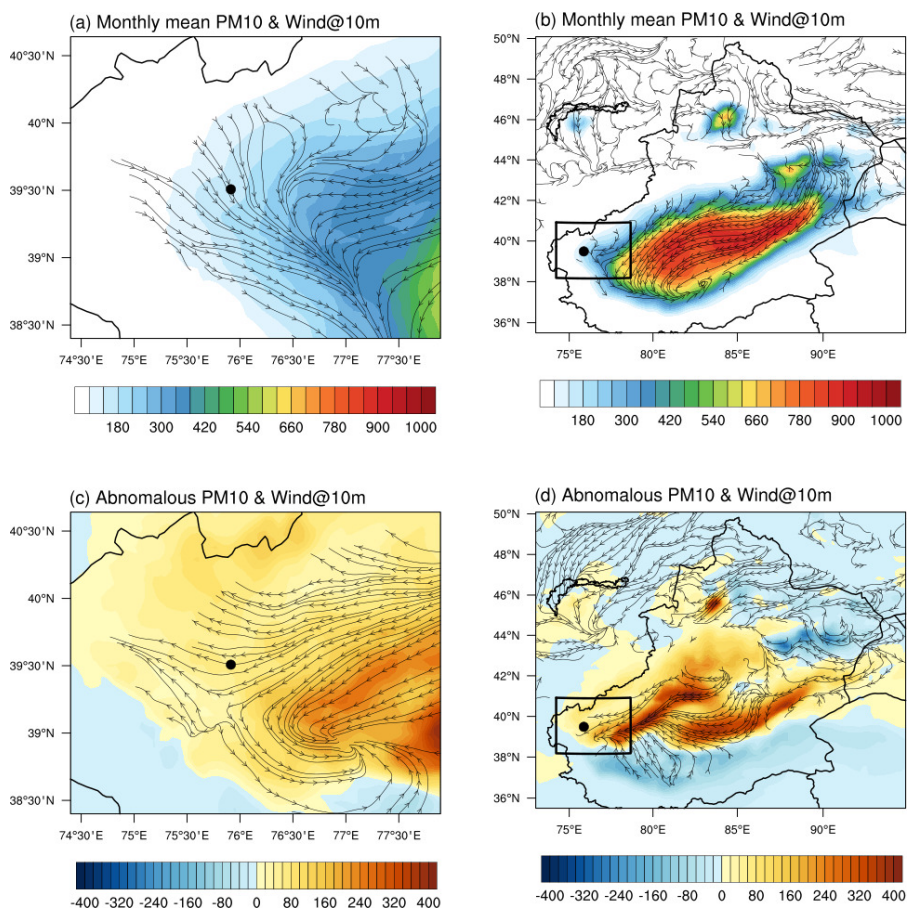


Figure 5. Monthly mean (a) PM₁₀ concentration ($\mu\text{g m}^{-3}$) and (b) the streamlines of the 10-m wind (m s^{-1}) in April and their daily mean anomalies (c, d) during a dust storm on 24 April to the monthly mean values. Only the streamlines at the topographical height lower than 2500 meters are shown for clarity. The rectangles in figures (b) and (d) denote the fine model domain 2, which was the geographical range in the figures (a) and (c). The black points indicate the Kashi city.

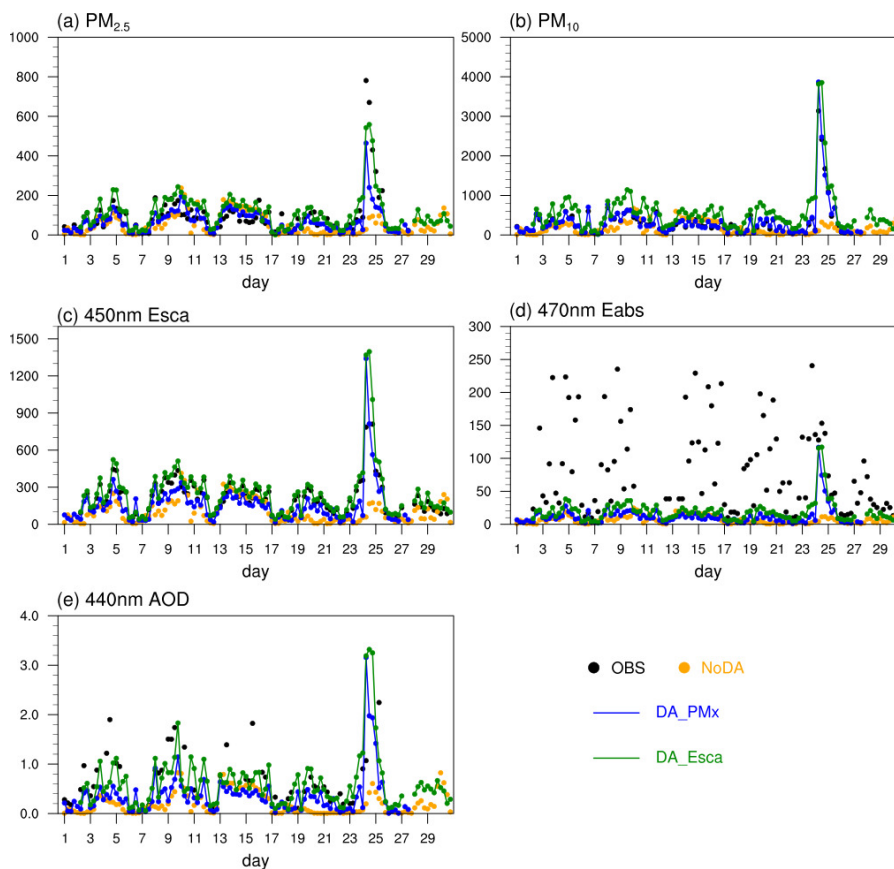


Figure 6. Comparison of (a) $PM_{2.5}$ ($\mu\text{g m}^{-3}$), (b) PM_{10} ($\mu\text{g m}^{-3}$), (c) aerosol scattering coefficient (Esca, Mm^{-1}), (d) aerosol absorption coefficient (Eabs, Mm^{-1}) and (e) AOD in the observation (OBS), the background simulation (NoDA), and the DA analyses when assimilating the observed $PM_{2.5}$ and PM_{10} (DA_PMx) and aerosol scattering coefficients (DA_Esca) at Kashi in April 2019.

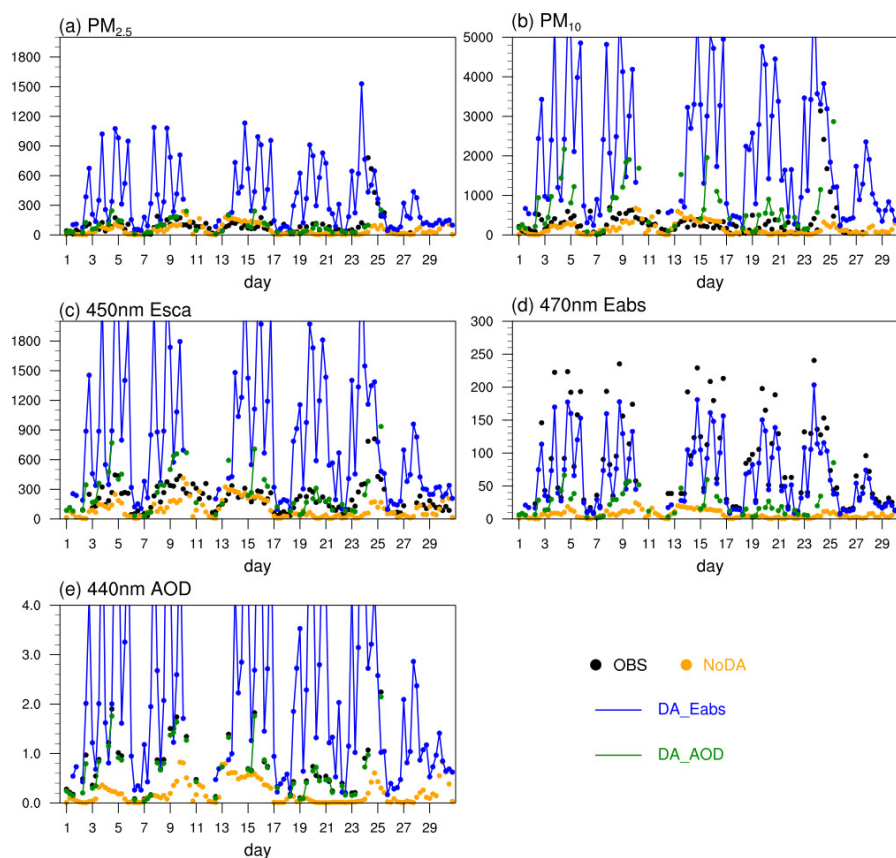


Figure 7. Comparison of (a) $\text{PM}_{2.5}$ ($\mu\text{g m}^{-3}$), (b) PM_{10} ($\mu\text{g m}^{-3}$), (c) aerosol scattering coefficient (Esca, Mm^{-1}), (d) aerosol absorption coefficient (Eabs, Mm^{-1}) and (e) AOD in the observation (OBS), the background simulation (NoDA), and the DA analyses when assimilating the observed aerosol absorbing coefficients (DA_Eabs) and AOD (DA_AOD) at Kashi in April 2019.

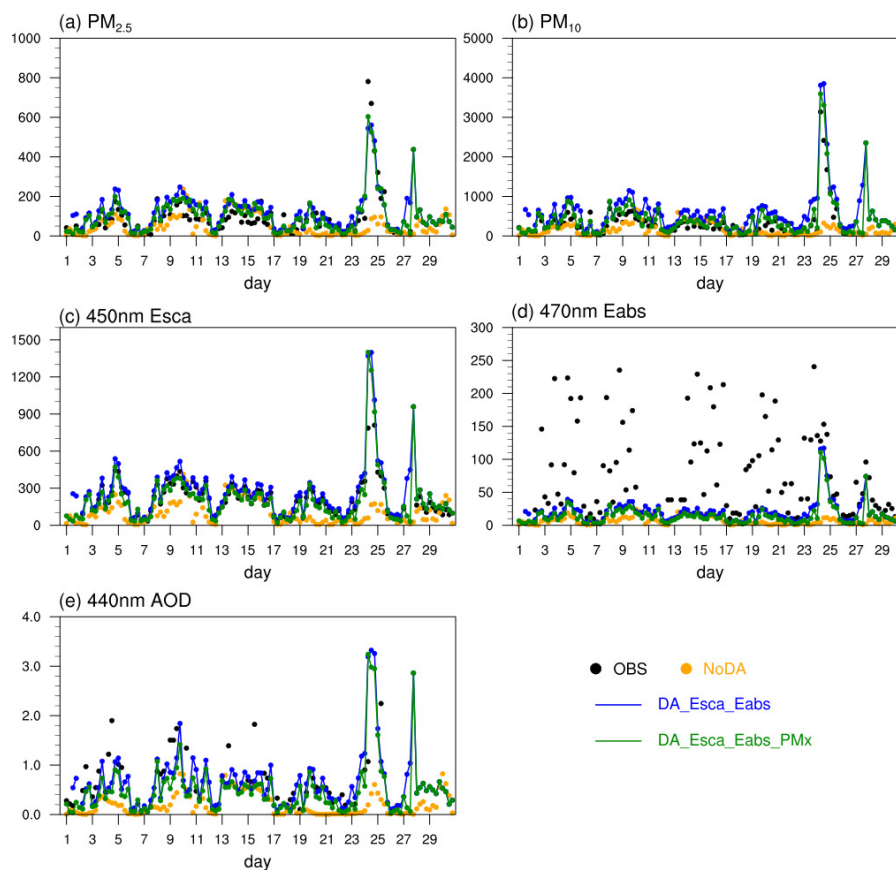


Figure 8. Comparison of (a) PM_{2.5} ($\mu\text{g m}^{-3}$), (b) PM₁₀ ($\mu\text{g m}^{-3}$), (c) aerosol scattering coefficient (Esca, Mm^{-1}), (d) aerosol absorption coefficient (Eabs, Mm^{-1}) and (e) AOD in the observation (OBS), the background simulation (NoDA), and the DA analyses of DA_Esca_Eabs and DA_Esca_Eabs_PMx at Kashi in April 2019.

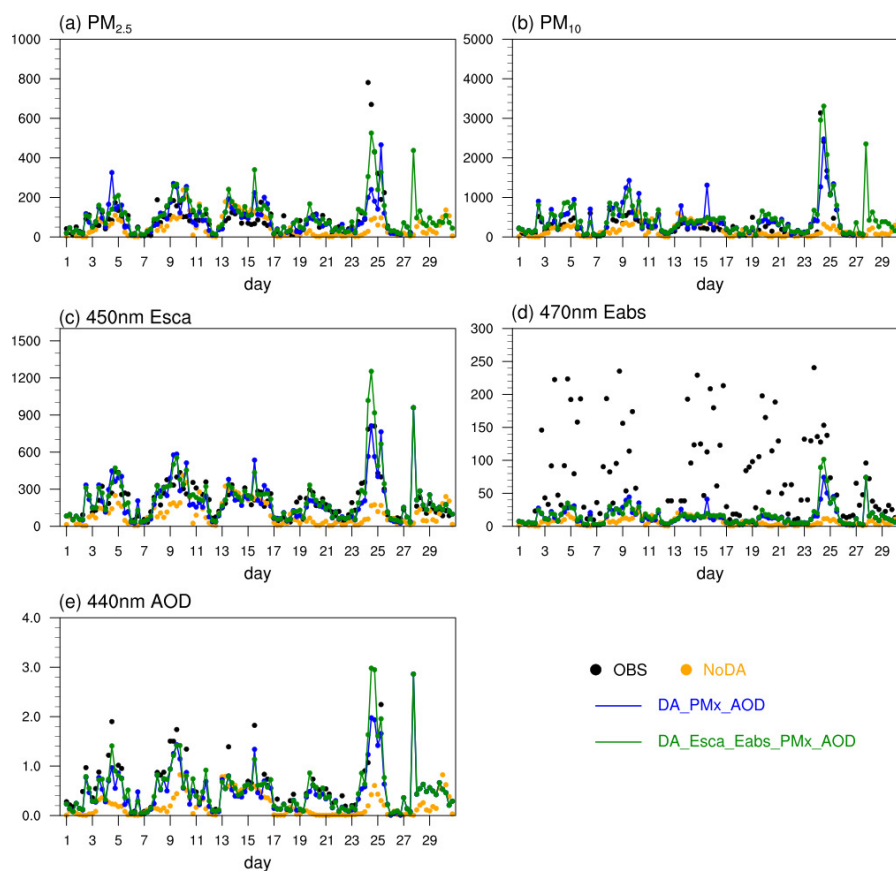


Figure 9. Comparison of (a) $\text{PM}_{2.5}$ ($\mu\text{g m}^{-3}$), (b) PM_{10} ($\mu\text{g m}^{-3}$), (c) aerosol scattering coefficient (Esca, Mm^{-1}), (d) aerosol absorption coefficient (Eabs, Mm^{-1}) and (e) AOD in the observation (OBS), the background simulation (NoDA), and the DA analyses of DA_PMx_AOD and DA_Esca_Eabs_PMx_AOD at Kashi in April 2019.

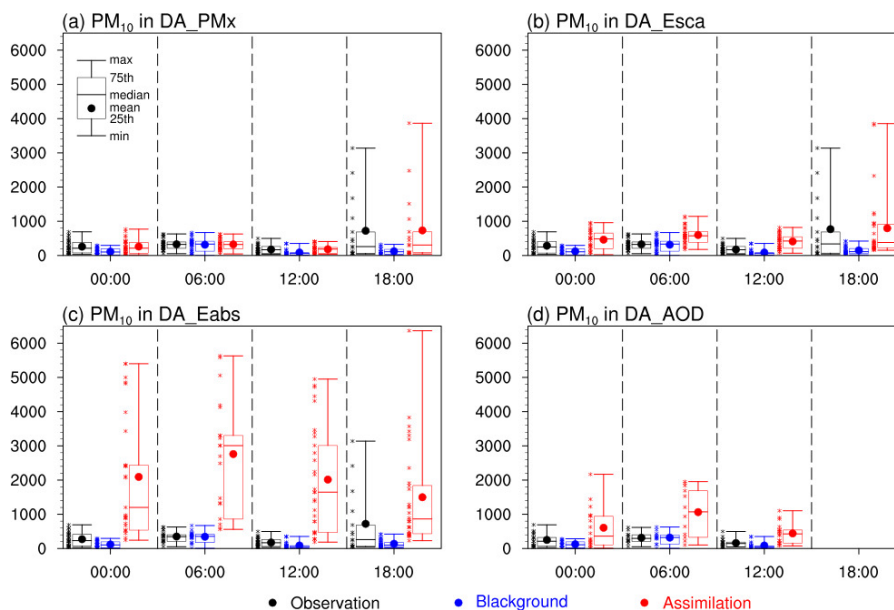


Figure 10. Surface PM_{10} concentrations ($\mu\text{g m}^{-3}$) in the observation (black), background simulation (blue) and the DA analyses (red) at 00:00, 06:00, 12:00, 18:00 UTC in April when assimilating the observations of (a) PM_x , (b) aerosol scattering coefficients (Esca), (c) aerosol absorption coefficient (Eabs), and (d) AOD, respectively. The DA_AOD had no analysis at 18:00 UTC that was local midnight. Kashi is 6 hours ahead of UTC (UTC+6).

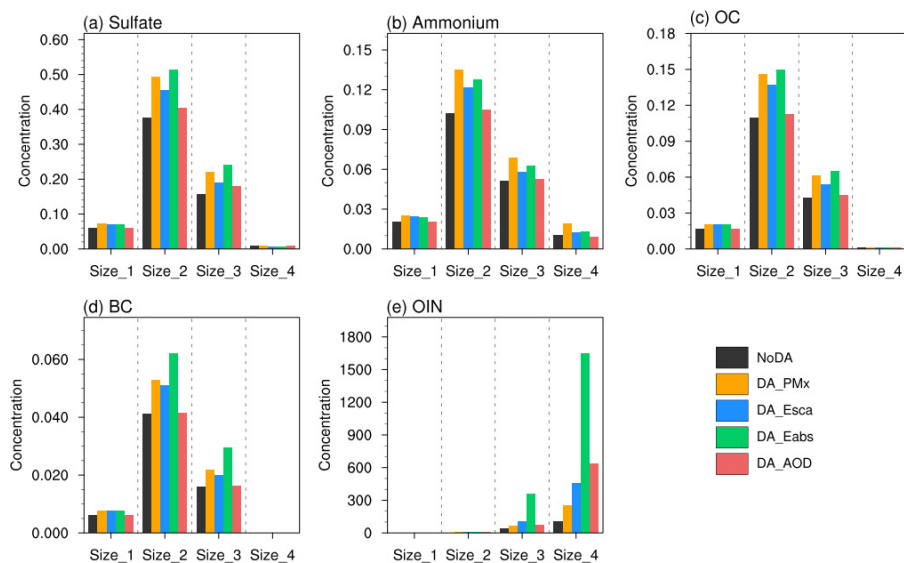


Figure 11. Monthly mean aerosol concentrations ($\mu\text{g m}^{-3}$) per size bin in the background (NoDA) and the DA experiments when assimilating the individual observation at Kashi in April 2019.

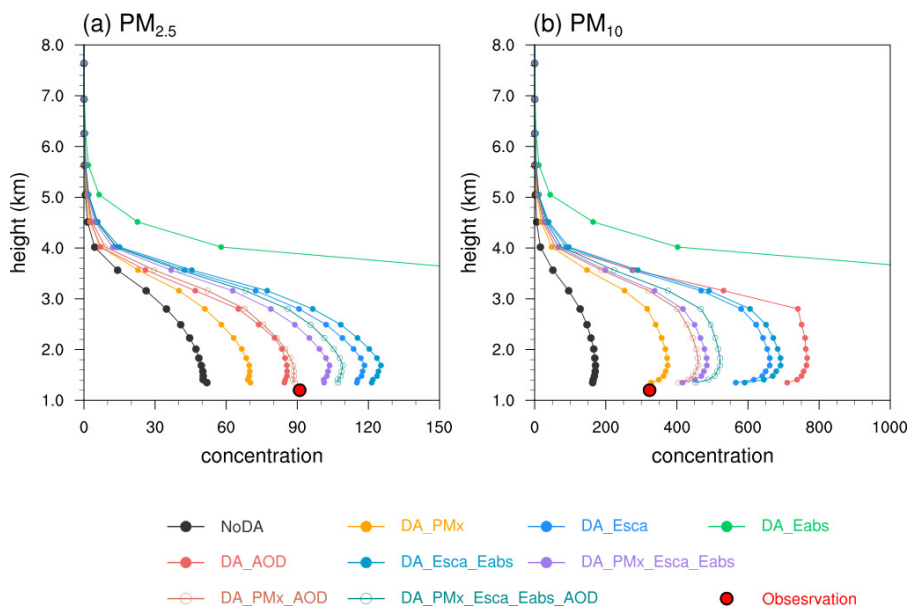


Figure 12. Monthly mean vertical concentration profiles of (a) $PM_{2.5}$ ($\mu\text{g m}^{-3}$) and (b) PM_{10} ($\mu\text{g m}^{-3}$) at Kashi in April 2019.



Figure 13. Monthly mean chemical composition in percent (%) in the PM₁₀, excluding the OIN component at Kashi in April 2019.



Table 1. The observed surface particle concentration, aerosol scattering coefficient (Esca), aerosol absorption coefficient (Eabs), and AOD used for the DA analysis and their observational errors.

	Data time range	Wavelength (nm)	Observation error (e)
PM _{2.5} & PM ₁₀ ($\mu\text{g m}^{-3}$)	Apr 1 – Apr 30		$e = \sqrt{e_1^2 + e_2^2}$ $e_1 = 1.5 + 0.75 \cdot PM_x$ $e_2 = 0.5 \cdot e_1 \cdot \sqrt{\frac{d}{3000}}$ <p>d: grid spacing in meter</p>
AOD	Mar 29 – Apr 25	440, 675, 870, 1020	$e = 0.01/\text{height} \times 10^8$
Esca (Mm^{-1})	Apr 2 – Apr 30	450, 525, 635	$e = 10$
Eabs (Mm^{-1})	Apr 2 – Apr 30	470, 520, 660	$e = 10$



Table 2. The monthly mean values of the PM_{2.5} and PM₁₀ concentrations ($\mu\text{g m}^{-3}$), 450 nm aerosol scattering coefficient (Esca, Mm^{-1}), 470 nm aerosol absorption coefficient (Eabs, Mm^{-1}) and 440 nm AOD in the background and analysis data and their correlation values (in brackets) with the observations at 00:00, 06:00, 12:00, 18:00 UTC at Kashi in April 2019. The underlined number in bold denotes the analysis in the monthly mean value that is not significantly different from the observation. The number in the bracket is the significant correlation, and the dashed line denotes an insignificant correlation. Both the statistical tests of the mean and correlation are conducted at the significance level of 0.05.

DA experiment	PM _{2.5} ($\mu\text{g m}^{-3}$)	PM ₁₀ ($\mu\text{g m}^{-3}$)	Esca (Mm^{-1})	Eabs (Mm^{-1})	AOD
Observation	91.0	323.2	204.5	81.9	0.70
Background	53.1 (0.23)	166.9 (-----)	106.5 (0.37)	6.7 (0.33)	0.18 (0.58)
Analysis					
DA_PMx	<u>70.3</u> (0.86)	<u>331.2</u> (0.99)	158.9 (0.86)	12.2 (0.33)	0.31 (0.37)
DA_AOD	<u>85.0</u> (0.33)	716.9 (0.35)	280.1 (0.58)	23.1 (0.16)	<u>0.63</u> (0.99)
DA_Esca	120.5 (0.93)	596.2 (0.96)	<u>244.6</u> (0.97)	19.1 (0.48)	<u>0.57</u> (0.47)
DA_Eabs	395.1 (0.31)	2161 (0.31)	849.0 (0.65)	65.1 (0.99)	1.95 (-----)
DA_Esca_Eabs	122.9 (0.92)	604.4 (0.93)	247.7 (0.97)	20.0 (0.46)	<u>0.58</u> (0.47)
DA_PMx_Esca_Eabs	<u>101.1</u> (0.93)	<u>411.2</u> (0.98)	<u>198.8</u> (0.92)	15.2 (0.38)	0.41 (0.47)
DA_PMx_AOD	<u>89.5</u> (0.51)	<u>408.8</u> (0.75)	<u>195.8</u> (0.74)	14.9 (0.32)	<u>0.51</u> (0.95)
DA_PMx_Esca_Eabs_AOD	<u>107.9</u> (0.77)	452.9 (0.94)	<u>216.3</u> (0.92)	16.2 (0.38)	<u>0.53</u> (0.93)



Table 3. The ratios of AOD, aerosol scattering/absorption coefficient to PM_{10} concentration (mean \pm standard deviation) in the observations, the model background data, and the DA analysis when assimilating surface particle concentrations (DA_ PM_x).

	Ratios of 440 nm AOD to PM_{10} ($\mu g^{-1} m^3$)	Ratios of 450 nm aerosol scattering coefficient to PM_{10} ($Mm^{-1} \mu g^{-1} m^3$)	Ratios of 470 nm aerosol absorption coefficient to PM_{10} ($Mm^{-1} \mu g^{-1} m^3$)
Observation	0.0033 \pm 0.0021	0.91 \pm 0.05	0.42 \pm 0.36
Background	0.0011 \pm 0.0007	0.68 \pm 0.24	0.05 \pm 0.02
Analysis	0.0012 \pm 0.0005	0.58 \pm 0.21	0.04 \pm 0.01



Table 4. The mean instantaneous clear-sky shortwave (SW), longwave (LW) and the net (SW+LW) direct radiative forcing (Wm^{-2}) at the top of atmosphere (TOA), in the atmosphere (ATM) and at the surface (SRF) in the background and the simulations restarted from the analyses of DA_PMx and DA_PMx_AOD at one hour after the analysis times of AOD DA at Kashi in April 2019.

	SW (Wm^{-2})			LW (Wm^{-2})			SW+LW (Wm^{-2})		
	TOA	ATM	SRF	TOA	ATM	SRF	TOA	ATM	SRF
Background	-7.8	+11.3	-19.1	+0.6	-3.6	+4.2	-7.2	+7.7	-14.9
DA_PMx	-8.7	+21.7	-30.4	+1.1	-7.4	+8.5	-7.6	+14.3	-21.9
DA_PMx_AOD	-12.2	+32.1	-44.3	+1.7	-12.6	+14.3	-10.5	+19.5	-30.0